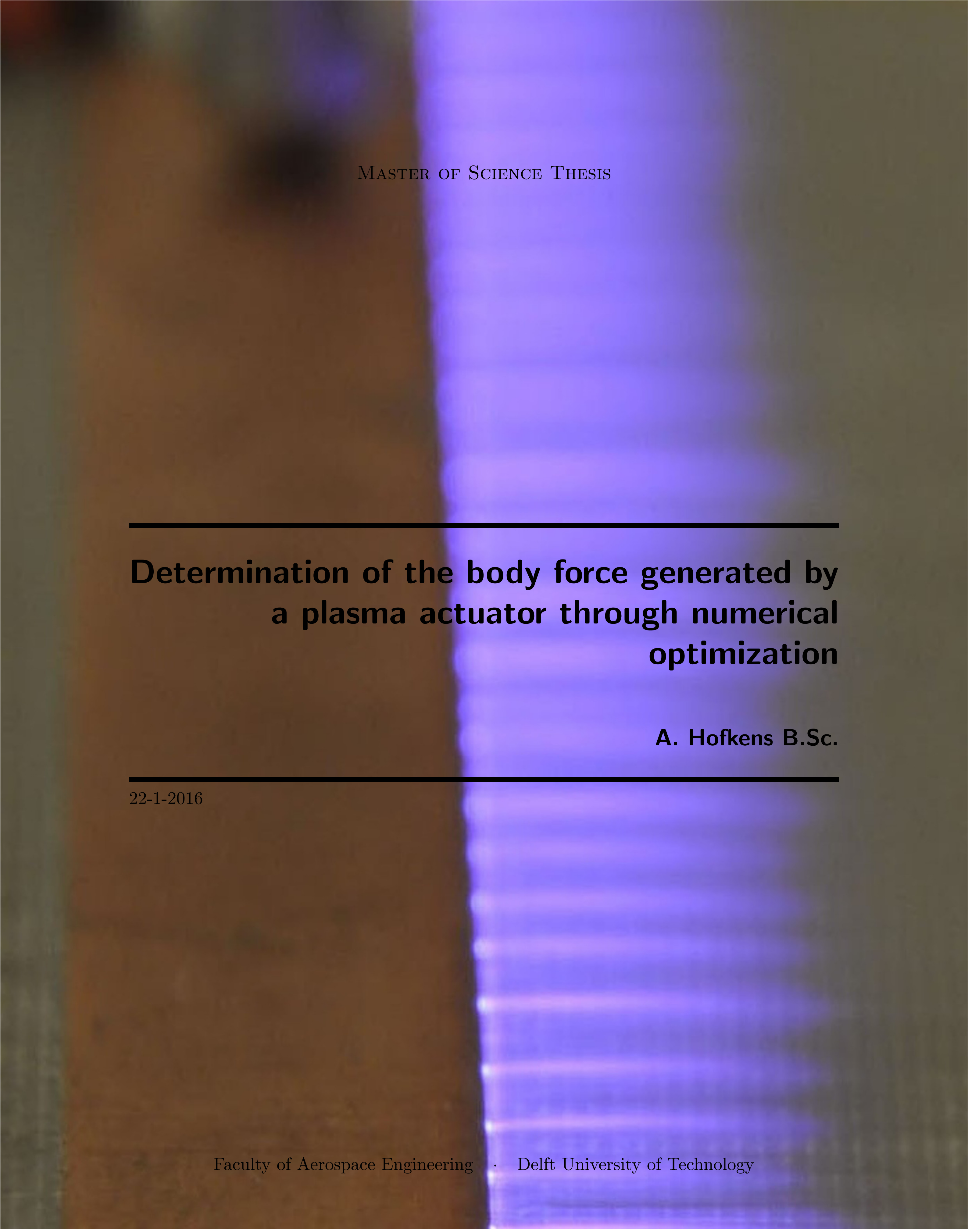

Master of Science Thesis

Determination of the body force generated by a plasma actuator through numerical optimization

A. Hofkens B.Sc.

22-1-2016

Faculty of Aerospace Engineering · Delft University of Technology

Delft University of Technology

Challenge the future

Determination of the body force generated by a plasma actuator through numerical optimization

Master of Science Thesis

For obtaining the degree of Master of Science in Aerospace Engineering at Delft University of Technology

A. Hofkens B.Sc.

22-1-2016

Faculty of Aerospace Engineering · Delft University of Technology

Cover picture by Experimental AeroScience Group - Temasek Labs - National University of Singapore

Delft University Of Technology
Department Of
Aerodynamics

The undersigned hereby certify that they have read and recommend to the Faculty of Aerospace Engineering for acceptance a thesis entitled **"Determination of the body force generated by a plasma actuator through numerical optimization"** by **A. Hofkens B.Sc.** in partial fulfillment of the requirements for the degree of **Master of Science**.

Dated: 22-1-2016

Head of department: ____________________
prof.dr. S. Hickel

Supervisor: ____________________
dr. M. Kotsonis

Reader: ____________________
dr. R.P. Dwight

Reader: ____________________
dr. D. Ragni

Summary

In order to extract the body force field that is generated by a plasma actuator from velocity data, most researchers disregard the influence of the pressure gradient to obtain a spatial and temporal description of the body force field. There is however some discussion whether this assumption is valid or not. The current research tries to compute the body force field by using a numerical optimization procedure, using a Matlab optimization routine combined with an OpenFOAM® solver which was adapted to accommodate for the body force term.

Many simplifications had to be made to be able to perform the optimization in a reasonable amount of time, among which were a fairly coarse numerical grid, a first order discretisation scheme and a parametrization of the body force field. Due to this last simplification, no real conclusions can be drawn with regard to the spatial distribution of the body force, but the integral body forces in x- and y-direction display more or less valid behaviour and correspond to previous research. It is also shown that the pressure gradient has the same order of magnitude as the body force density in all 8 cases, which means that this research challenges the assumption that the pressure gradient is of little importance when trying to obtain the body force from velocity data.

Acknowledgements

First and foremost, I wish to thank my supervisor Marios Kotsonis for always being available and ready to help whenever I had any questions. There was not a moment when I had the feeling I was bothering him, although I am sure he sometimes had a lot of more important things on his mind. I am very grateful for that.
Secondly I want to thank my parents for giving me the opportunity to study in Delft and being patient as I kept moving the deadline of my thesis further and further into the future. Studying Aerospace Engineering in Delft and doing my internship in Italy was truly a great experience and it would not have been possible without their continuing support.
Furthermore I would like to thank my Belgian friends with whom I spent all those years in Delft. They were always ready to give advice or to take my mind of things when I ran into problems with my thesis or my study altogether.
Lastly I want to thank everyone in the Aerodynamics lab for the occasional coffee, my international friends in Delft for the occasional beer and my sister and two brothers for reminding my parents that they should not worry that much about why I still hadn't graduated. At least now you can say your brother is an aerospace engineer!

Delft, The Netherlands A. Hofkens B.Sc.
22-1-2016

Contents

List of Figures

List of Tables

Nomenclature

Latin Symbols

C_L	lift coefficient	–
$\mathbf{f}$	body force vector $[f_x\ f_y\ f_z]^T$	N
f	frequency	Hz
h	normalized cell spacing	–
$\mathbf{k}_{i,j}$	control point for Bézier surface at (i, j)	–
L	global norm of the discretisation error	–
n	number of cells	–
p	pressure	Pa
$\widehat{p}$	order of numerical scheme	–
r	ratio between cell spacings	–
r	refinement ratio	–
t	time	s
$\mathbf{u}$	velocity vector $[u_x\ u_y\ u_z]^T$	m/s
V	voltage	V

Greek Symbols

α	angle of attack	rad
ε	discretisation error	–
μ	dynamic viscosity	Pl
ρ	volumetric mass density	kg/m^3

ω	vorticity	1/s

Subscripts

$_x$	in x-direction
$_y$	in y-direction
$_z$	in z-direction

Superscripts

$^+$	positively charged
$^-$	negatively charged

Abbreviations

2D	two-dimensional
AC	alternating current
CFD	computational fluid dynamics
CPU	central processing unit
DBD	dielectric barrier discharge
HOT	higher order terms
HWA	hot-wire anemometry
LDA	laser Doppler anemometry
N-S	Navier-Stokes
NACA	National Advisory Committee for Aeronautics
ns	nanosecond-pulsed
PISO	pressure implicit with splitting of operator
PIV	particle image velocimetry
ppm	parts per million
SDBD	single dielectric barrier discharge
ZNMF	zero-net mass flux

Other Symbols

dB	decibel
∇	del operator

N	nitrogen
O	oxygen

Chapter 1

Introduction

One of the most researched topics in the aerospace industry is the topic of flow control. For more than a century, researchers have tried to find means to alter the flow around an object to achieve a desired change in the effects generated by the airflow [19]. During this period, many flow control devices have been devised among which there are both passive devices such as vortex generators, and active devices such as boundary layer suction. Recently, many research efforts have been attributed to dielectric barrier discharge (DBD) plasma actuators. As the name suggests, these devices consist of two electrodes which are located at different streamwise positions and separated by a layer of a dielectric material. Some of their key advantages, such as their high frequency response, low complexity, a lack of moving parts, low weight and an ability to sustain high g-forces make them ideally suited for use in the aerospace industry [8].

Generally, there are two types of DBD plasma actuators. First of all, there is the nanosecond-pulsed DBD plasma actuator, or ns-DBD plasma actuator. This type of actuator generates a plasma that is sustained by repetitive, high-voltage pulses of very short duration - in the order of nanoseconds. These high-voltage pulses cause the surrounding air to undergo a sudden temperature rise due to an energy transfer from the actuator to the near-surface gas. A shock wave then emerges which, together with secondary vortex flows, redistributes the momentum of the main flow [45].

On the other hand, there is the AC-DBD plasma actuator, which is driven by an alternating current voltage signal. This high-voltage signal causes the air around the actuator to become weakly ionized. Under the influence of the electric field generated by the AC voltage signal, the ionized particles will start to move and collide with the neutral particles, causing the air to start moving near the surface [8, 16]. This process can also be described is the emergence of a body force field, generated by the moving ionized particles and acting upon the neutral particles. The problem is however that the quantification of this body force field proved to be rather difficult.

Many researchers have been trying to characterize the body force field generated by an AC-DBD plasma actuator. A popular approach is to take velocity and acceleration terms from for example PIV measurements and insert them into the Navier-Stokes equations, leaving only the pressure gradient term and the body force term as unknowns [63, 3, 30, 14, 39, 5, 37]. Most reseachers then go on to disregard the pressure gradient term, making it possible to extract the body force field directly from the PIV measurements [63, 39, 5, 37]. However, Kotsonis et al found with their method that the pressure gradient is far from negligible and their research thus challenges the method used by most of the researchers upto this day [30].

A better understanding of the magnitude and form of the body force field generated by an AC-DBD plasma actuator is of great importance to the field of aerodynamic flow control in that it allows researchers to perform numerical simulations to investigate the effect of plasma actuators on a particular flow field. An accurate representation of the body force field will generate valid numerical results far more quickly and at a lower cost than having to perform a complete experiment to acquire valid data for every configuration of the plasma actuator.

1.1 Research objectives

The purpose of this research is thus to characterize the body force field generated by an AC-DBD plasma actuator by performing a numerical optimization of the body force field, such that the resulting velocity field approximates a velocity field extracted from experiments. First of all, a new solver is created using the OpenFOAM® open-source CFD package, in order to deal with the addition of a body force field. This solver is then implemented into a MATLAB optimization routine and verified by calculating the observed order of the numerical discretisation method. Several numerical grids will be analysed and an optimal mesh will be chosen, after which different methods to parametrize the body force field will be investigated. An optimal configuration will then be used to find the body force field for several experimental velocity fields, in order to get an idea of the general layout and magnitude of a body force field generated by an AC-DBD plasma actuator.

1.2 Thesis outline

First of all, some background information will be provided in chapter 2. After that, the methodology will be explained in detail in chapter 3, followed by the verification and optimization of the mesh and surface parametrization in chapter 4. Results for 8 different velocity fields will be presented in chapter 5. Lastly, chapter 6 gives the conclusion and recommendations for further research.

Chapter 2

Background

Plasma actuators are a fairly new concept in the field of flow control. Researchers in the past decades have studied the effects of plasma actuators extensively and have proven that they have the potential to control the flow around airfoils such that higher lift coefficients and/or lower drag coefficients can be achieved [36, 6, 21]. This chapter gives an overview of different flow control concepts, after which it will discuss what plasma actuators are and how they are able to alter the flow field around an object. Lastly, an overview of the current research on the magnitude and distribution of the body force will be presented.

2.1 Aerodynamic flow control

According to Gad-el-Hak [19], flow control became a scientific field of research after Prandtl introduced his boundary later theory. Before that, efforts to control fluid flow were merely empirical. Think for example about the fins on the end of an arrow to stabilize it in flight. After the emergence of the boundary layer theory however, flow control research could be based on physical reasoning and the number of flow control devices increased steadily. The research into flow control devices grew further during the second world war and the worldwide energy crisis in the 1970s in an attempt to design faster, more maneuverable and more fuel efficient aircraft [19].

A distinction can be made between passive and active flow control devices, see figure 2.1. Passive flow control devices do not require additional energy input once they are installed. They thus cannot be controlled and alter the flow at all times, leading them to be sometimes termed 'flow management devices' instead of 'flow control devices' [18]. Examples of passive flow control devices are vortex generators [34, 53], which force the boundary to become turbulent and thereby postpone separation, or Gurney flaps [53], which enhance lift by effectively increasing the camber of an airfoil. Active flow control devices are true flow control devices in that they need additional energy input and can be controlled to operate whenever there is a benefit to be gained. Gad-el-Hak [19] further makes the distinction between active flow control devices where the input signal is predetermined or devices where

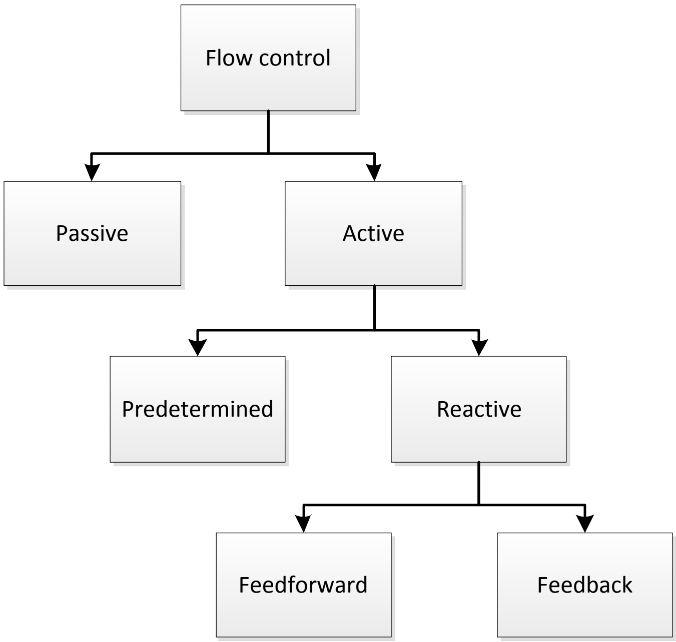

Figure 2.1: Breakdown of different flow control strategies.

the input signal reacts to the state of the flow. The control loop can then either be open (feedforward) or closed (feedback), see again figure 2.1.

Another way to categorize the different types of active flow control devices is according to their working principles, as done by Cattafesta & Sheplak [7]. They distinguish four types of active flow control devices: fluidic devices, moving object/surface devices, plasma devices and others, such as electromagnetic or magnetohydrodynamic devices.

Fluidic devices have the objective to provide fluidic injection into or fluidic suction from the main fluid flow. They can further be subdivided into devices that require no external fluid source and devices that do require an external fluid source. The first type is also often called a zero-net mass flux (ZNMF) device. Since they use no external fluid source, they need to alternately ingest and expel fluid from the fluid flow through a hole in the surface, using synthetic jet actuators such as piezoelectric diaphragms [20]. The devices that do require an external fluid source include amongst others pulsed jets [48, 49], operated by opening and closing a valve and releasing fluid from an external fluid container, and combustion actuators [13] which produce jets generated by a combustion process. These latter devices obviously have the disadvantage of requiring an external fluid source but they can cause larger perturbations in the flow or perturbations with higher velocities than the ZNMF devices.

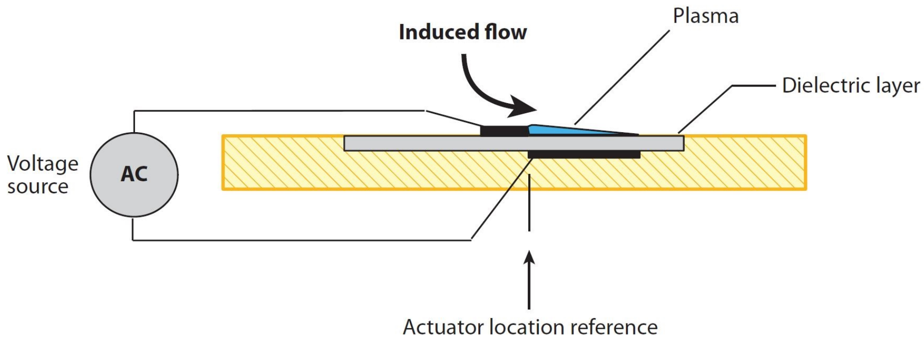

Figure 2.2: Configuration of an AC-DBD plasma actuator. [8, p.506]

Moving object/surface devices involve a geometric change inside the fluid domain or on its boundaries. This change in geometry has the objective to change the local fluid motion to for example postpone boundary layer separation. Examples of this type of devices include vibrating ribbons [28], vibrating flaps [26, 50], oscillating wires [4], rotating surfaces [59] and morphing surfaces [55].

Plasma devices use high voltages to partly ionize the surrounding air and gaining an advantage from the polarity of that air. They are typically lightweight, do not involve any moving parts which makes them inherently less complex than the other types of active flow control devices, and they have high frequency response times. The most popular plasma actuator is the single dielectric barrier discharge (SDBD) plasma actuator, which uses two electrodes separated by a dielectric barrier and positioned at different streamwise locations. The electrodes are then coupled to a high voltage source which either provides an AC voltage signal (an AC-DBD plasma actuator) or short high voltage pulses with a duration in the order of nanoseconds (an ns-DBD plasma actuator). The main disadvantage of SDBD plasma actuators is their diminishing control authority for increasing freestream velocities. Other plasma devices include the multiple DBD plasma actuator which tries to increase the produced body force, the local arc filament actuator which provides pressure perturbations through localized heating of the fluid and the sparkjet actuator which is able to produce jets of up 250 m/s [38].

2.2 Layout and working principles of an AC-DBD plasma actuator

An AC-DBD plasma actuator is actually a quite simple device. It consists of one electrode that is exposed to the air, a layer of dielectric material beneath it and another electrode under this dielectric barrier, as illustrated in figure 2.2.

As can be seen from figure 2.2, the electrodes are placed at a different streamwise position, with the covered electrode located further downstream than the exposed electrode. They are mostly just made out of thin[1] sheets of copper [17, 44, 56]. The dielectric barrier in

[1] In the order of a few hundreds of millimeters [17, 44, 56].

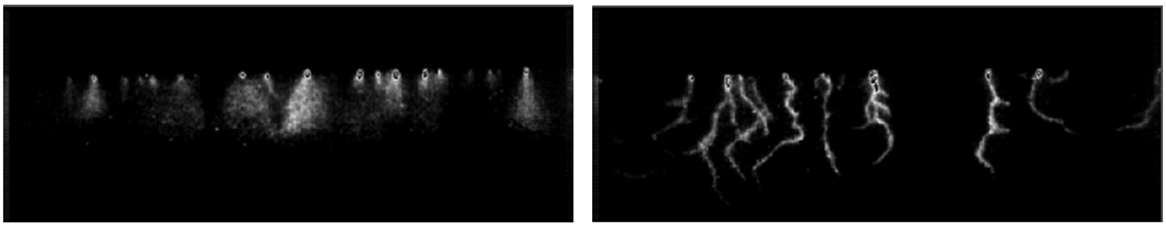

(a) Negative half-cycle. (b) Positive half-cycle.

Figure 2.3: Movement of electrons throughout the AC voltage cycle. [15, p.2738]

between the two electrodes is usually a thin sheet of Kapton, although other material such as Teflon, quartz and glass can also be used [17, 44, 56]. The electrodes are then coupled to a voltage source which puts the electrodes under an AC voltage, with peak-to-peak voltage amplitudes ranging from 2 kV [41] to 75 kV [56] and voltage frequencies ranging from 0.02 kHz [33] to 60 kHz [24].[2]

To better understand the physics behind the working mechanism of an AC-DBD plasma actuator, the AC voltage cycle is split up in two parts: a part where the exposed electrode is more negative than the covered electrode (the negative half-cycle) and a part where the exposed electrode is more positive than the covered electrode (the positive half-cycle).

In the negative half-cycle, the exposed electrode acts as a source of electrons. These electrons are then deposited on the dielectric surface in the vicinity of the exposed electrode [11, 52]. Because of this deposit of electrons on the dielectric barrier, the potential difference between the dielectric and the electrode is reduced. The deposition of electrons can thus be regarded as a self-limiting process. Therefore, the applied voltage has to increase constantly in order to deposit more electrons on the dielectric [16]. The deposition of electrons on the dielectric during the negative half-cycle is a quasi-steady process due to the 'infinite' supply of electrons. As can be seen in figure 2.3a, the area near the edge of the exposed electrode seams to 'glow', and the negative half-cycle is therefore also called the 'glow regime'.

During the positive half-cycle, the dielectric acts as a source of electrons for the exposed electrode. If the potential difference between the exposed electrode and the dielectric is large enough, the electrons will move from the dielectric surface to the electrode. The dielectric surface can however not be regarded as an infinite source of electrons. Furthermore it appears that the electrons have more difficulties separating from the dielectric than from the electrode, which results in a series of micro-discharges instead of a quasi-constant deposit [11, 52]. The irregular nature of the movement of electrons from the dielectric surface to the exposed electrode can also be seen in figure 2.3b. Because of this more irregular deposit and the resulting 'streams' of electrons that are apparent in figure 2.3b, the positive half-cycle can also be called the 'streamer regime'.

Due to the presence of the high voltage, the air surrounding the AC-DBD plasma actuator gets weakly ionized with an ion density that is typically less than 1 ppm [8]. Both positive (N_2^+ and O_2^+) and negative (O^- and O_2^-) ions are present in the plasma region, but according to numerical simulations performed by Singh & Roy [51], the density of positive ions is

[2]Ranges for the peak-to-peak voltage amplitudes and the voltage frequencies are taken from a topical review by Kotsonis [29].

much higher than the density of negative ions. Furthermore, they found that the density of positive ions is higher during the positive half-cycle than during the negative half-cycle, which implies that more ions move from the exposed electrode towards the covered electrode (negative during the positive half-cycle) than the other way around. Ion-neutral collisions then cause the rest of the surrounding atoms to start moving along with the ions, causing an 'electric wind' in the direction of the covered electrode. It should be noted that the effect of the movement of the electrons is regarded as negligible, as electrons are far smaller than ions and electron-neutral collisions thus have a negligible impact [32].

2.3 Applications of plasma actuators

Because of their ability to alter the flow around an object, low weight, high frequency response times and easy integration and operation, plasma actuators can be used for a wide range of applications. A number of these are explained in this section.

2.3.1 Separation control

Corke & Post [10] attached a plasma actuator to the leading edge of an airfoil, with the covered electrode located on the suction side and the exposed electrode located on the pressure side of the airfoil. Several airfoils were used for testing, including the NACA 0009, NACA 0012, 66_3-018 and the HS3412. Chord-based Reynolds numbers ranged from 77.000 to 460.000, with free-stream velocities varying from 10 to 30 m/s. Three operating modes for the plasma actuator were used. First, the plasma actuator was turned off. Secondly, the plasma actuator was turned on and the voltage waveform had a frequency of 3-10 kHz and a peak-to-peak amplitude of 7-12 kV. This mode was termed the 'steady' mode. Thirdly, an 'unsteady' mode was used in which the plasma actuator was turned on and turned off alternately. The 'on'-time lasted for about 10% of the 'off'-time. The resulting $C_L - \alpha$ curves can be found in figure 2.4.

It can be seen that the stall angle for an airfoil without plasma actuator is approximately 14°, which increases to about 18° when the plasma actuator is turned on in 'steady' mode. When turned on in 'unsteady' mode, the results are even better as the stall angle increases to 22° and the maximum value for C_L jumps from 1.3 to 1.4. The results were also found to be consistent with the numerical simulations performed by Voikov et al [60], which are represented by the solid and dashed lines in figure 2.4. In a later study, Corke showed that by using a plasma actuator at the leading edge, the lift-to-drag ratio could be improved with 340% [21].

Leading edge separation control was also applied on gas turbine blades by Huang et al [23]. A plasma actuator was installed slightly ahead of the separation location and operated again in both 'steady' and 'unsteady' modes. Both operating modes were effective, as the 'steady' mode caused the laminar boundary layer to become turbulent and the 'unsteady' mode created spanwise flow structures, which promoted turbulent mixing of the flow.

Little et al [35] applied a plasma actuator on the hinge of the deflected flap of a high-lift airfoil to reduce the separation region behind the deflected flap. Using the plasma actuator in 'steady' mode, no real improvement in lift coefficient was found and the separation region

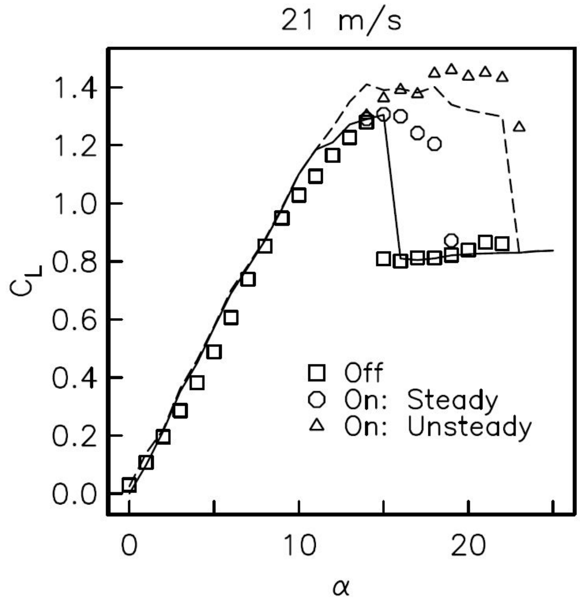

Figure 2.4: $C_L - \alpha$ curves for different operating modes of a plasma actuator attached to the leading edge of an airfoil. [10, p.2172]

appeared to be elongated, although starting at a point further downstream. The 'unsteady' mode proved to be more effective, as the separation was shortened because of enhanced momentum transfer between the separation region and the freestream.

2.3.2 Roll control

He et al [21] investigated the effects of installing a plasma actuator near the trailing edge of an airfoil. If the plasma actuator was operated in 'steady' mode as defined by Corke & Post [10], the actuator behaved somewhat as a plain trailing edge flap. If plasma actuators were to be located on the trailing edge of both sides of the wing along 30% of the wing span, a roll moment could be generated equal to a deflection of 2.5° of the ailerons of a normal wing. When the plasma actuators would cover the entire span of the wing, the resulting roll moment would be equivalent to deflecting the ailerons by 9°. According to He et al, it would thus certainly be possible to use plasma actuators for flight corrections during cruise instead of using the ailerons, thereby gaining an advantage from the fact that plasma actuators have no moving parts. Since there are then also no hinge gaps or corners which the airflow can encounter, drag during the cruise phase of a flight can be reduced by using plasma actuators for roll control.

Also Vorobiev et al [61] investigated the possibility of using plasma actuators for roll control. They positioned a plasma actuator on each side of the wing at 75% of the chord and applied a sawtooth voltage signal with a frequency of 2.9 kHz and a peak-to-peak amplitude of 32 kV. They found that it was possible to achieve a roll moment equivalent to an aileron deflection of 3° at a freestream velocity of 2 m/s when only one of the two plasma actuators was turned on. When both actuators were turned on, the resulting roll moment was zero but there was an increase in the lift coefficient of almost 0.1, as can be seen in figure 2.5.

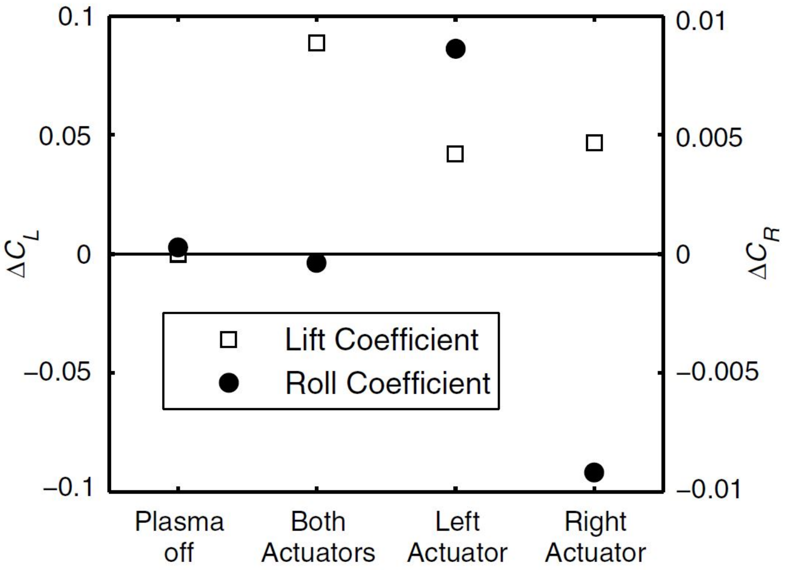

Figure 2.5: Lift and roll control by combined operation of plasma actuators at both sides of the wing. [61, p.1320]

2.3.3 Noise control

With the objective to try to reduce the noise caused by a landing gear of a commercial transport aircraft, Thomas et al [57] attached four DBD plasma actuators to the downstream part of a circular cylinder. Testing at a diameter-based Reynolds number of 33.000 and a free-stream velocity of 4 m/s, they found that they could eliminate Karman vortex shedding when turning on the plasma actuators, see figure 2.6. Furthermore, the separation levels are reduced drastically, which in turn reduces the velocity deficit in the wake of the cylinder and the width of the wake. Also turbulence levels are reduced with about 80% compared to the wake of a cylinder without plasma actuators.

Using microphone measurements, Thomas et al found that the near field sound pressure levels could be reduced by as much as 13.3 dB when numerically integrating the power spectral density from 6 to 10 Hz with the actuator turned both on and off. However, since in reality the Reynolds number will be of the order 10^6 and the geometric complexity of a landing gear system is far greater than just a cylinder, the body force generated by the plasma actuator will need to be increased to achieve the same promising results.

2.3.4 Other applications

Besides separation control, roll control and noise control, plasma actuators are also suitable for numerous other applications. For example Jukes et al [25] use plasma actuator to obtain a 45% reduction in skin-friction drag by generating a spanwise flow oscillation in the near-wall region of the turbulent boundary layer. Wilkinson [64] investigated the same method to reduce skin-friction drag but achieved only a 40% decrease. Another mechanism to reduce skin-friction drag was used by Whalley & Choi [62], who introduced spanwise travelling waves into the turbulent boundary layer using DBD plasma actuators. They managed to

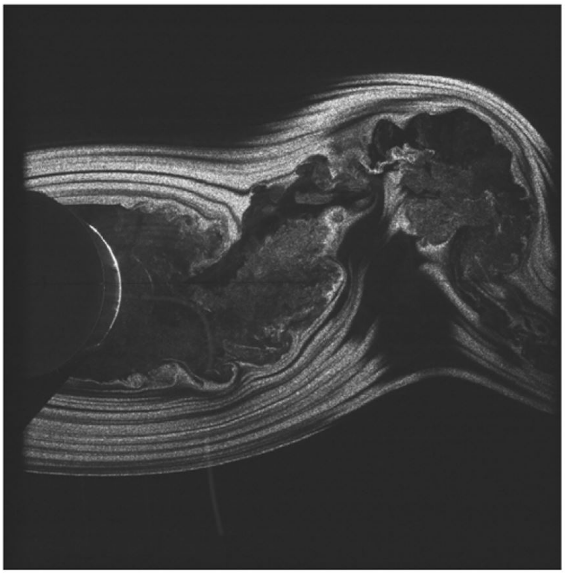

(a) Plasma actuator turned off.

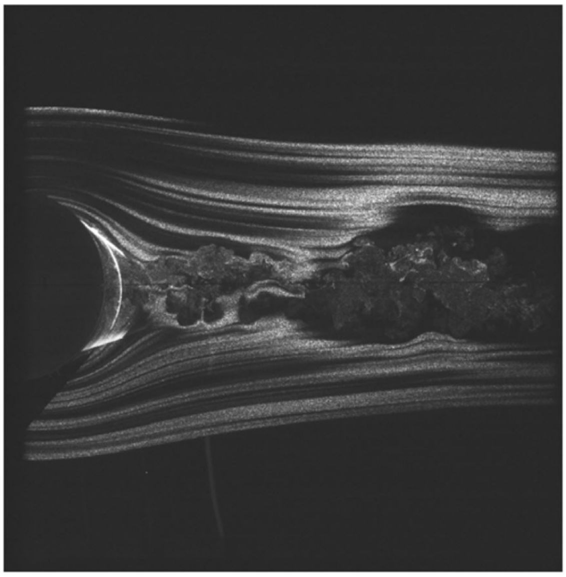

(b) Plasma actuator turned on.

Figure 2.6: Near-wake flow visualization off a circular cylinder. [57, p.1924-1925]

decrease the skin-friction drag with about 30%.

Yet another application of plasma actuators is increasing the lift coefficient using circulation control. Zhang et al [65] performed numerical simulations of a wall jet introduced at the trailing edge of an airfoil. The pressure difference between the suction side and the pressure side of the airfoil was increased due to the addition of the wall jet, reaching an increase in the lift coefficient that is similar to more conventional circulation control techniques.

Samimy et al [47] used localized arc filament plasma actuators to introduce streamwise vortices into an axisymmetric or rectangular nozzle in order to manipulate high-speed jets. Lastly, also Corke & Matlis [9] applied plasma actuators for jet control, more particularly to control the exciting helical modes in an axisymmetric jet. Corke & Matlis managed to reduce the rms fluctuations in the jet while the time-averaged jet velocity did not change that much.

2.4 Determination of the steady body force generated by an AC-DBD plasma actuator

The body force generated by a plasma actuator is hard to determine directly from experiments. One approach is to measure the space-integrated force using load cell measurements or momentum balance analyses, but they don't measure the pure body force since they incorporate wall friction forces. Moreover, for implementation in numerical solvers, a spatial distribution of the body force is required. Efforts have been made to find such a spatial distribution, but again it is hard to find the pure body force field from experiments. To see why this is the case, the 2D incompressible Navier-Stokes momentum equation is presented in equation (2.1):

$$\rho\left(\frac{\partial \mathbf{u}}{\partial t}+\mathbf{u}\cdot\nabla\mathbf{u}\right)=-\nabla p+\mu\nabla^2\mathbf{u}+\mathbf{f} \tag{2.1}$$

This equation consists of terms in **u**, p and **f**. Experiments like particle image velocimetry (PIV), laser Doppler anemometry (LDA) and hot-wire anemometry (HWA) measure the velocity throughout the experimental domain but can not discern between the contribution of the pressure gradient and the contribution of the body force. Many researchers have been trying to find solutions for this problem, but there is still some disagreement about which solution is the most acceptable. The different methods used to determine the body force field from velocity measurements will be presented in section 2.4.1, after which an analysis of the different methods will be made in section 2.4.2.

Although the body force distribution will vary across an AC voltage cycle, this section will first consider a time-averaged and thus steady version of the body force. This steady body will not yield as accurate results as a fully time-resolved description of the body force, but it can give a first approximation of the effects of an AC-DBD plasma actuator.

2.4.1 Overview of existing methods for determining the body force

A short overview of the most important literature regarding the determination of the steady body force generated by an AC-DBD plasma actuator will be given in this section in order to create a better understanding of the difficulties in describing the steady body force.

Wilke [63] was one of the first to propose a method to obtain the body force from velocity field data such as PIV measurements. The velocity field data and its spatial and temporal derivatives can be inserted into the Navier-Stokes momentum equation (2.1), leaving only the pressure gradient term and the body force term unknown. In order to then separate the body force term from the pressure gradient term, Wilke assumes that the pressure gradient is negligible compared to the body force. The method is subsequently validated by inserting the obtained body force into an incompressible fluid solver and comparing the resulting velocity field with the measured velocity field. Wilke found the method to be valid but as the pressure gradient term is neglected in his method, the calculated body force is actually a combination of the body force and the pressure gradient (whether negligible or not). Inserting this body force into a fluid solver will produce the original velocity field with a zero-valued pressure gradient throughout the domain, as the pressure gradient is included in the body force term. The validation method used by Wilke is thus not sound and the pressure gradient term might not be negligible after all.

Albrecht et al [3] tried to obtain the body force field without neglecting the pressure term by using the velocity-vorticity formulation of the momentum equation, as is shown in equation (2.2):

$$\frac{1}{\rho}\left(\frac{\partial f_x}{\partial y}-\frac{\partial f_y}{\partial x}\right)=\frac{\partial \omega}{\partial t}+u\frac{\partial \omega}{\partial x}+v\frac{\partial \omega}{\partial y}-\nu\left(\frac{\partial^2\omega}{\partial x^2}+\frac{\partial^2\omega}{\partial y^2}\right) \tag{2.2}$$

By rewriting the momentum equation in terms of the vorticity ω, which is defined as $\frac{\partial v}{\partial x} - \frac{\partial u}{\partial y}$, the pressure term is eliminated. However, there are now two terms to describe the body force and only one equation, so the assumption is made that the streamwise component of the force is larger than the wall-normal component. As such, it can be written that $\frac{\partial f_x}{\partial y} - \frac{\partial f_y}{\partial x} \approx \frac{\partial f_x}{\partial y}$ and the streamwise body force component can be extracted from PIV data. Albrecht et al validated their method by comparing numerical simulations with experimental data, and found that the method gives good agreement for the body force if the body force consists mainly of the streamwise component. If there is also a wall-normal component, the agreement is not so good but the calculated body forces still have a correct value for the curl. Furthermore, Albrecht et al's method require highly accurate velocity measurement since there are third-order derivatives involved in the calculation method.

Another method to derive the body force from PIV measurements is proposed by Kotsonis et al [30]. As a basis, they use the Navier-Stokes momentum equation as given in equation (2.1). The plasma actuator is first placed in a box where quiescent conditions hold. There is thus a zero pressure gradient and no external flow. Kotsonis et al assume that in the first moment after starting the actuator, these conditions still hold and the pressure gradient, convective terms and viscous terms can be neglected. This results in the following equation, termed the 'reduced method' by Kotsonis et al:

$$\rho \frac{\partial \mathbf{u}}{\partial t} = \mathbf{f} \tag{2.3}$$

After that, it is assumed that the body force term does not change in time and is thus quasi-steady. Although it is known to Kotsonis et al that the body force does fluctuate in time, the body force term can be regarded as steady over a large number of voltage cycles as the time scale of the AC voltage cycle is usually much smaller than the time scale of the 'hydrodynamic inertia' of the flow [30, p. 2]. The momentum equation (2.1) can now be differentiated in time to give following equation:

$$\rho \left(\frac{\partial^2 \mathbf{u}}{\partial t^2} + \frac{\partial}{\partial t} \left(\mathbf{u} \cdot \nabla \mathbf{u} \right) \right) = \frac{\partial}{\partial t} \left(-\nabla p + \mu \nabla^2 \mathbf{u} \right) \tag{2.4}$$

The body force term has disappeared from this equation since it is assumed to be quasi-steady and its derivative in time is thus zero. When integrating equation (2.4) back in time, an expression for the pressure gradient can be found:

$$\int_0^t \left[\frac{\partial}{\partial t} \left(\mu \nabla^2 \mathbf{u} \right) - \rho \left(\frac{\partial^2 \mathbf{u}}{\partial t^2} + \frac{\partial}{\partial t} \left(\mathbf{u} \cdot \nabla \mathbf{u} \right) \right) \right] = \nabla p + C \tag{2.5}$$

As it is assumed that prior to the actuation the pressure gradient is zero, the integration constant C can be set to zero. This way, an expression for the pressure gradient is found and can be inserted into the momentum equation (2.1), after which the body force field can be found. This method was termed the 'gradient method' by Kotsonis et al. In figure 2.7, the body force field is displayed for a range of voltages and frequencies. It can be seen that as the voltage amplitude increases, the magnitude of the force increases and the body force field extends towards the covered electrode. Increasing the frequency does not change the shape of the body force field significantly as only the magnitude of the body force increases.

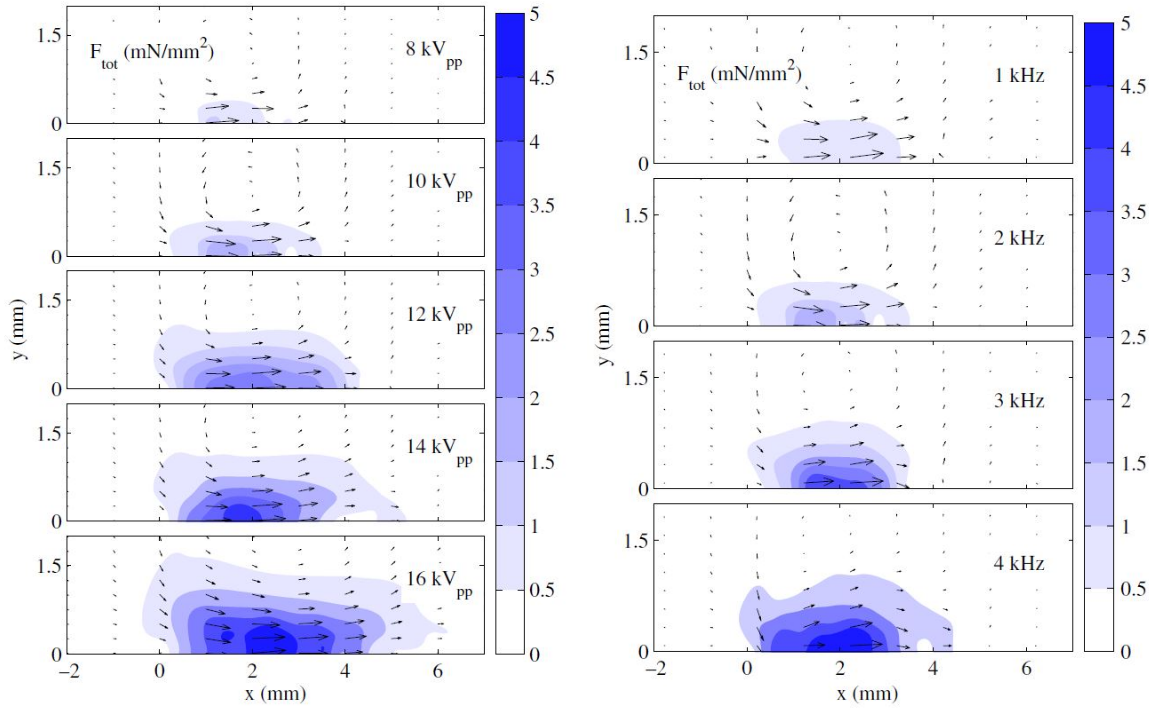

(a) Body force field with varying voltage amplitudes and fixed voltage frequency of 2 kHz.

(b) Body force field with varying voltage frequencies and fixed voltage amplitude of 10 kV.

Figure 2.7: Body force fields for varying peak-to-peak amplitudes and frequencies of the AC voltage cycle. [30, p.8]

Using their method, Kotsonis et al also investigated the influence of the different terms of the momentum equation (2.1) to the generation of the body force. They found the acceleration terms to be dominant in the first moments after actuation, validating the use of the 'reduced method' in those first moments (0.5 ms). After that, the pressure gradient term and the convective terms become dominant, while the viscous terms stay small throughout the entire time span as can be seen in figure 2.8.

Kotsonis et al validated their method using force measurements and a momentum balance analysis. They found the body forces calculated using their method to be consistently higher than the forces measured using the load cell or the momentum balance analysis. This discrepancy can be attributed to the fact that the load cell and momentum balance method measure the net force produced, which is essentially the body force minus the wall friction forces.

A comparison of several body force estimation techniques was performed by Kriegseis et al [31]. They divide the force estimation techniques into integral and differential approaches, with the integral approaches providing a value for the space-integrated body force and the differential approaches being able to describe the entire body force field. Comparing the integral techniques, it is found that the wall friction has a large influence on the measured force, up to 30%. For the differential approach, Kriegseis et al compare the method where the pressure gradient is neglected with the method that uses the velocity-vorticity formulation

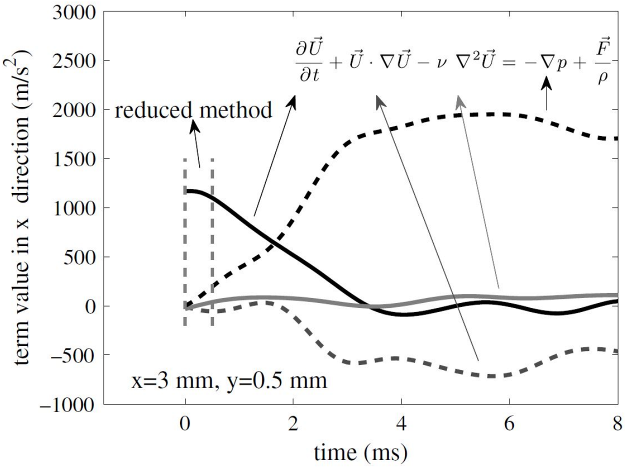

Figure 2.8: Contribution of the separate terms of the momentum equation to the generation of the body force for a peak-to-peak voltage amplitude of 12 kV and a frequency of 2 kHz. [30, p.7]

and only takes into account the streamwise component of the body force. For both methods, the 10% isolines are calculated as the line which connect the points where the horizontal force component is 10% as large as the maximum force. The result can be seen in figure 2.9. Clearly, the two methods give fairly similar results from which Kriegseis et al conclude that the influence of the pressure gradient term is at least one order of magnitude smaller than the intensity of the total volume force. They further conclude that the convective terms are dominant in both cases, much more so than the diffusive terms.

2.4.2 Comparison of existing methods for determining the body force

The most common method to determine the body force generated by a plasma actuator is the method first devised by Wilke [63], which uses the Navier-Stokes momentum equation (2.1) and discards the pressure gradient term. Wilke found his method to be valid by inserting the calculated body force into a fluid solver, but since the calculated body force is actually the body force and the pressure gradient combined, this validation method is not sound. Albrecht et al [3] use a different approach by rewriting the momentum equation into the velocity-vorticity equation (2.2) and taking into account only the streamwise component of the force. They found that whenever the force field is composed mainly out of streamwise forces, their method is valid. When the wall-normal component of the force gets too large however, the method of Albrecht et al fails although the resulting forces have the correct curl. Lastly there is the method of Kotsonis et al [30], which combines a 'reduced method' (equation (2.3)) in the first few moments after actuation and a 'gradient method' (equation (2.5)) in the later stages, which assumes the body force field to be quasi-steady and the pressure gradient to be zero before actuation. In contrast to what is assumed by Wilke [63], Kotsonis and his colleagues find that the pressure gradient is far from negligible in the production of the body force and they thus question the validity of Wilke's assumption. On the other hand, Kriegseis et al [31] compared the method of Wilke [63] with the method of Albrecht et al [3] and found the extension of the body force field to be fairly similar for both methods, concluding that the pressure gradient term can indeed be neglected.

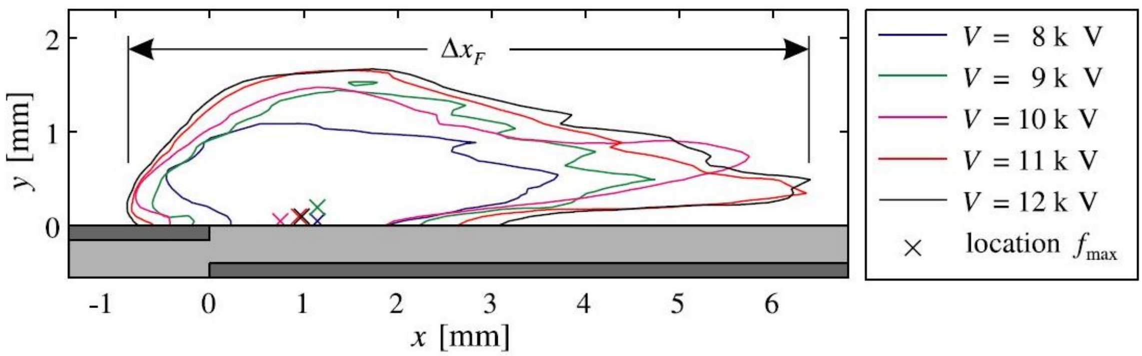

(a) Method based on Navier-Stokes momentum equation

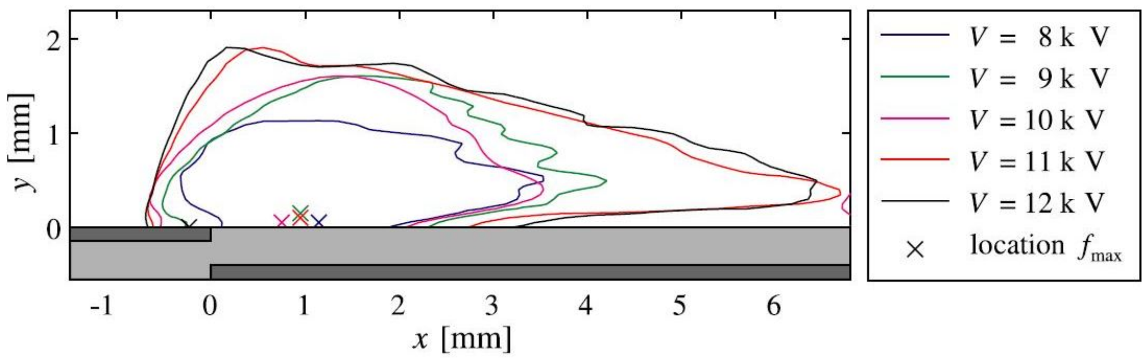

(b) Method based on velocity-vorticity formulation

Figure 2.9: 10% isolines for the streamwise body force component f_x for several voltage amplitudes and a frequency of 11 kHz. [31, p. 11]

Chapter 3

Methodology

In order to fully understand the method used to optimize the body force field, a flow chart of the entire optimization routine is presented in figure 3.1. It can be seen in the flow chart that the optimization routine consists out of three different main building blocks: the initialization of the body force field using a Bézier surface build up from Bernstein polynomials, the solving of the flow field resulting from the implemented body force field, and the optimization of the Bernstein coefficients such that the body force field generates a flow field that most closely matches a flow field obtained from experiments. These three main building blocks will be elaborated upon in section 3.1, section 3.2 and section 3.3 respectively.

3.1 Parametrization of the body force field

The region in the computational domain where the body force will be implemented consists of many mesh points, which each needs to be assigned a different value for the body force in x- and y-direction. Optimizing the body force at all these mesh points would take far too much computation time, so the body force field needs to be parametrized as a surface in order to speed up the optimization routine.

The choice was made to use a Bézier surface, build up from Bernstein polynomials, to approximate the body force field. Bézier surfaces are mathematical splines which are defined by a set of control points and are build up from Bernstein polynomials. They have the property that they pass through the outer control points and they are very easy to implement, making them perfectly suitable for the parametrization of the body force field.

The Bézier surface of degree $n \times m$ is defined on a unit square ($[\,0\;1\,] \times [\,0\;1\,]$) and has $(n+1) \times (m+1)$ control points $\mathbf{k}_{i,j}$. The definition of the Bézier surface can be found in equation (3.1):

$$\mathbf{f}(x,y) = \sum_{i=0}^{n} \sum_{j=0}^{m} B_i^n(x)\, B_j^m(y)\, \mathbf{k}_{i,j} \tag{3.1}$$

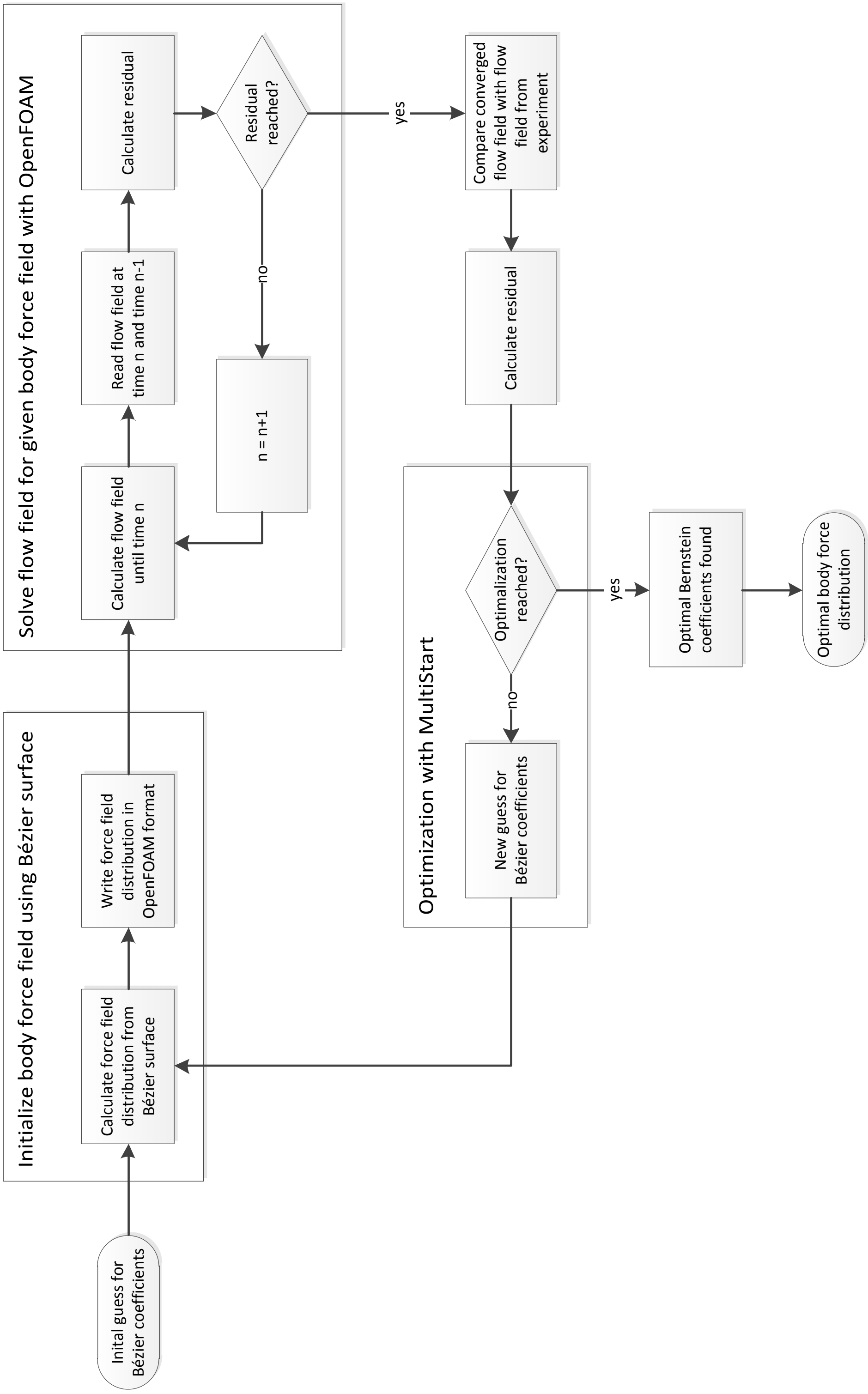

Figure 3.1: Flow chart of the optimization of the body force field.

In equation (3.1), $B_i^n(x)$ and $B_j^m(y)$ are Bernstein polynomials, defined according to equation (3.2).

$$B_i^n(x) = \binom{n}{i} x^i (1-x)^{n-i} \tag{3.2}$$

with $\binom{n}{i} = \frac{n!}{i!(n-i)!}$ being the binomial coefficient.

The control points at the edge of the body force field are chosen to be zero, such that there is a gradual transition from the region where the body force applies to the rest of the computational domain. Note that for every control point, a value for the calculation of the body force field in x-direction and one for the calculation of the body force field in y-direction needs to be specified. So for a Bézier surface of degree $n \times m$, a number of $2(n-1)(m-1)$ control variables need to be specified.

To implement the body force field in the computational domain (see also section 3.2), a number of tasks have to be executed. First, the cell numbers where the body force needs to be applied are extracted from the mesh using the *topoSet* utility. After having gathered the cell numbers and their coordinates, the coordinates are converted such that they span a unit square area. The body force components can now be calculated for each point on the unit square and each cell number is assigned a value for the body force in x- and y-direction. Lastly, the body forces are written to the input file using the *setFields* utility.

3.2 The OpenFOAM software package

A numerical solver had to be selected in order to calculate the flow field resulting from the implementation of the body force. For the purpose of this research, the OpenFOAM® software package was chosen simply because it is an open-source CFD solver. It was important to use an open-source solver because the code needed to be adapted to be able to incorporate body forces into the Navier-Stokes equations, since in most cases those body forces are neglected and left out of the Navier-Stokes equations. This section will first describe the case, its boundary conditions and the used mesh, after which the solver will be discussed together with the choice for the discretisation scheme.

3.2.1 Case, mesh and boundary conditions

The case examined in this project is the application of an AC-DBD plasma actuator on a flat plate in quiescent conditions, as illustrated in figure 3.2.

As can be seen in figure 3.2, the region where the body force applies is very small compared to the computational domain, as it stretches from -2 to +8 mm in x-direction and from 0 to +2 mm in y-direction. This region was chosen based on previous research peformed by Kotsonis et al [30] and Kriegseis et al [31], who both estimated the spatial distribution of the body force for similar peak-to-peak voltage amplitudes and frequencies as will be investigated in this project (see also section 2.4).

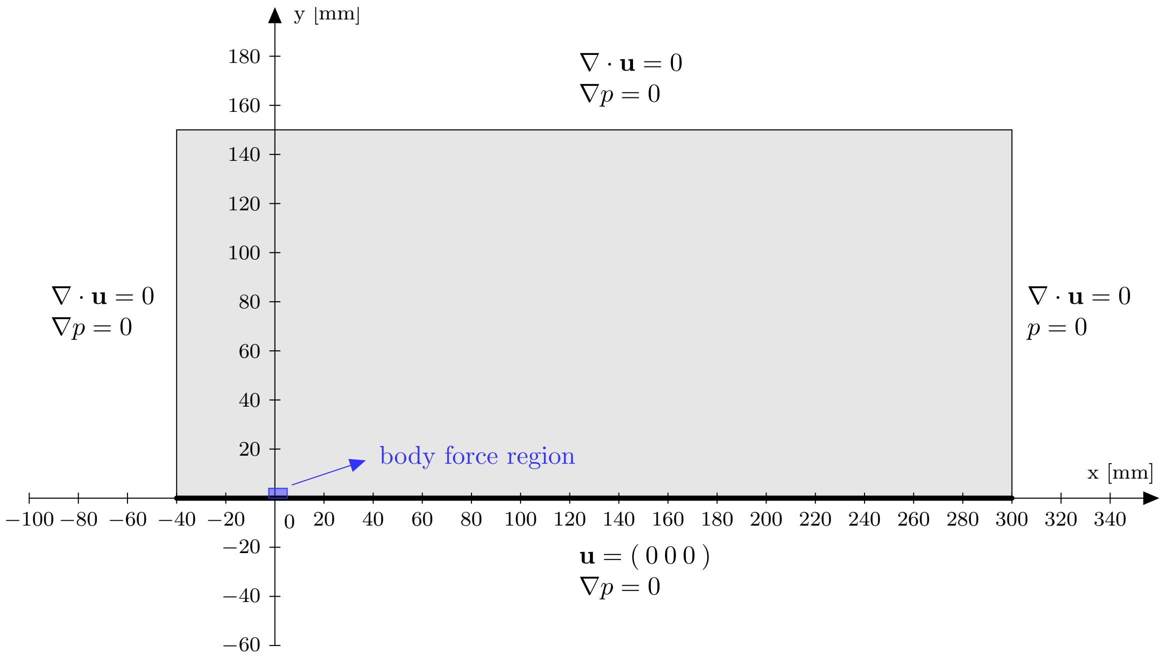

Figure 3.2: Case domain and boundary conditions. Plasma actuator is located at the origin.

The mesh was generated with OpenFOAM® and was designed to have more cells in the vicinity of the body force region and gradually larger cells when moving away from the body force region. An example of the mesh can be found in figure 3.3.

The mesh from figure 3.3 will be scaled up to investigate the influence of the mesh size on the optimized body force distribution. Furthermore, the mesh will be optimized to try to reduce the number of cells while ensuring the solution is still accurate. This will be further discussed in section 4.2.

The boundary conditions at the top and the left side of the domain are chosen such that the gradient of both the velocity and the pressure is zero. At the plate, the velocity is fixed at zero in all directions, while the pressure gradient is again zero. Finally at the right side, the gradient of the velocity is zero, while the pressure is prescribed as zero. The right side of the computational domain is thus defined as a pressure outlet.

3.2.2 The *icoFoamBF* solver & discretisation scheme

According to their website, OpenFOAM® "has an extensive range of features to solve anything from complex fluid flows involving chemical reactions, turbulence and heat transfer, to solid dynamics and electromagnetics" [40]. To solve the flow field resulting from the application of an AC-DBD plasma actuator however, a basic solver for laminar, incompressible flow can be used since the flow velocity is typically not larger than 10 m/s and the flow stays laminar for the entire length of the plate. Therefore, the *icoFoam* solver was used to solve the flow field. *icoFoam* solves the flow field according to the PISO algorithm, which uses the

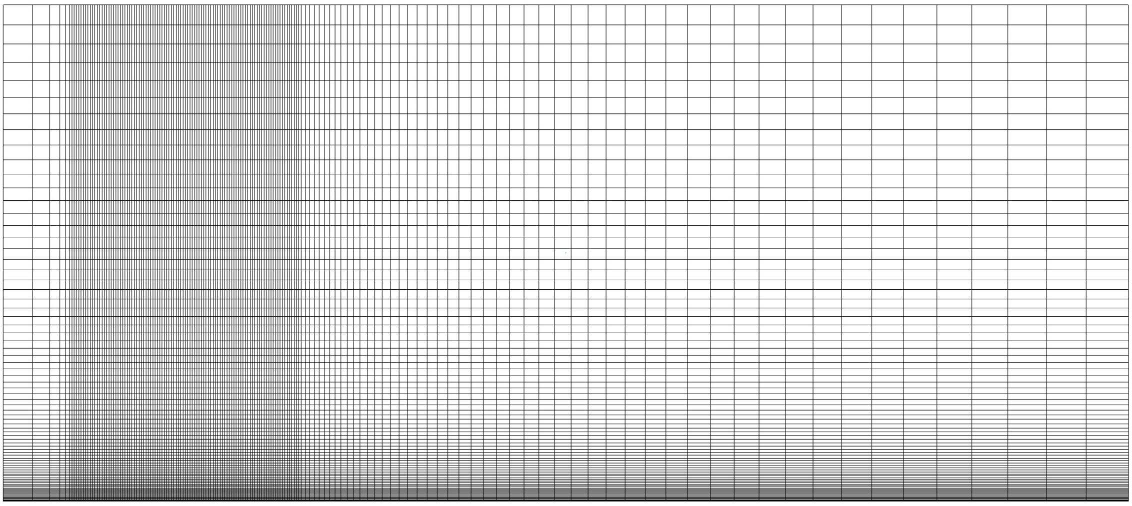

Figure 3.3: Layout of the coarse mesh.

Navier-Stokes (N-S) momentum equation (3.3) to calculate the velocity field:

$$\rho\left(\frac{\partial \mathbf{u}}{\partial t}+\mathbf{u}\cdot\nabla\mathbf{u}\right)=-\nabla p+\mu\nabla^2\mathbf{u} \tag{3.3}$$

However, *icoFoam* clearly does not incorporate body forces into the N-S momentum equation. The *icoFoam* solver was therefore adapted to include body forces according to equation (3.4). This solver is termed *icoFoamBF*.

$$\rho\left(\frac{\partial \mathbf{u}}{\partial t}+\mathbf{u}\cdot\nabla\mathbf{u}\right)=-\nabla p+\mu\nabla^2\mathbf{u}+\boxed{\mathbf{f}} \tag{3.4}$$

The spatial discretisation is done using an upwind scheme. Although upwind schemes are only first order schemes, they are much more stable which proved to be necessary for solving the flow field for every kind of body force distribution the optimization scheme 'throws' at the solver. The number of cells needed to ensure stability and avoid non-physical oscillations when using a central difference scheme proved to be too large, so the upwind scheme was chosen despite being only a first order scheme. The better stability of the upwind scheme can be attributed to the fact that it introduces 'numerical dissipation', dissipation that is non-physical but is introduced through the discretisation of the N-S momentum equation. In general, numerical dissipation should be kept to a minimum since it attributes to inaccurate results. However, it occurs only when the flow is not aligned with the primary axis of the grid [58]. Since the plasma actuator produces a flow that is parallel to the plate, numerical dissipation should not violate the results to a large degree. To ensure that this is indeed the case, the effect of numerical dissipation will be estimated for different sizes of the grid. Subsequently, the mesh will be optimized to try to reduce the effect of numerical dissipation in section 4.2.

The time step that is used during the calculations is adjustable and submitted to the criterion that the maximum Courant number can not be higher than 0.9. see equation (3.5):

$$C_{max} = \frac{u \cdot \Delta x}{\Delta t} < 0.9 \tag{3.5}$$

The condition that the Courant number can never get larger than 1 prohibits a fluid particle to travel further than the distance between two cells during one time interval, and is a necessary but not a sufficient condition for convergence [12]. It was chosen to set the maximum Courant number to 0.9 instead of 1, small enough to ensure the solver would never use a time step that caused the Courant number to get larger than 1 in some cells but on the other hand still large enough such that the time step is not unnecessarily small and thereby slowing down the optimization.

The convergence criterion for each run of the *icoFoamBF* solver can be found in equation (3.6):

$$\frac{\max\left(\mathbf{u}^n - \mathbf{u}^{n-1}\right)}{\max\left(\mathbf{u}^n\right) \cdot \Delta t} \leq 10^{-4} \tag{3.6}$$

In order to check whether the convergence criterion is met or not, the solver is ran until the next write step (e.g. 0.25 seconds of simulated time), after which the velocities of the current and the previous time step are extracted and the residual is calculated. When the condition is not met, the solver runs again starting from the latest time. When the convergence condition is met for both the velocities in x-direction and the velocities in y-direction, the flow field is considered to have converged.

The resulting flow field is than compared to a benchmark flow field obtained from experiments according to equation (3.7):

$$\varepsilon = \overline{\mathrm{mag}\left(\mathbf{u} - \mathbf{u}_b\right)} \tag{3.7}$$

It is chosen to take the mean of the magnitude of the difference in every cell between the computed flow field and the benchmark flow field as the optimization objective, because it is a good measure to quantify the resemblance between the computed flow field and the benchmark flow field and can be optimized relatively fast. A downside of trying to minimize the mean of the residuals of every cell is that a small residual in one cell can compensate a large residual in another cell. Therefore the computed flow field might have another topology than the benchmark flow field, but the mean velocity will still be approximately the same. Another option was to take the maximum residual as an optimization objective and thus try to minimize the maximum difference between the computed flow field and the benchmark flow field. In this case however, it is possible that the computed flow field is very close to the benchmark flow field except for a couple of cells in which the residual is large. The optimization procedure will then continue to optimize the body force field even though the two flow fields are already very similar. The optimization procedure will thus take more time than needed when taking the maximum difference as optimization objective and therefore the mean of the residuals was taken as optimization objective to reduce the computation time.

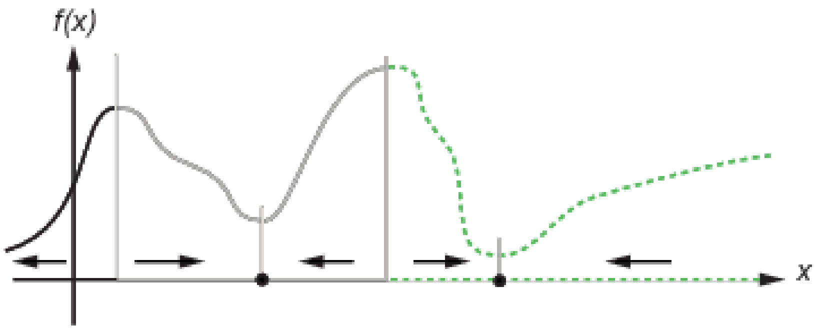

Figure 3.4: Illustration of basins of attraction [54].

3.3 The MultiStart optimization routine

The optimization routine that was used to find the best set of Bézier coefficients is the `MultiStart` routine which is implemented in MATLAB [54]. It is designed to find a global mininum by running another MATLAB optimization routine, called `fmincon`, locally on multiple starting points.

`MultiStart` was chosen over another MATLAB optimization routine that is designed to find a global minimum called `GlobalSearch`. `GlobalSearch` also runs `fmincon` on multiple starting points but first checks whether the starting point under consideration is worth running `fmincon` on. It does that by estimating the extent of the basin of attraction, as illustrated in figure 3.4. When a starting point lies within the same basin of attraction of another starting point where `fmincon` has already found a solution, `GlobalSearch` does not run the local solver on the starting point.

The reason why `GlobalSearch` was not chosen is that it examines starting points throughout the whole domain of possible solutions, whereas with `MultiStart` the starting points can be submitted to certain constraints. It can for example be chosen to only use starting points which generate a body force field that has a net body force which is positive in the x-direction. This way, examining the solver for infeasible starting points is avoided and the optimization can be performed much faster. This was also found by two studies performed at the Uppsala University in Sweden by Agnarsson et al [2] Hendra & Adinugroho [22], who investigated several optimization methods implemented in MATLAB for their accuracy and speed. It was found that both `GlobalSearch` and `MultiStart` are able to find the global minimum, but `MultiStart` is able to find it three times as fast as `GlobalSearch`. Furthermore, they found that the `sqp` algorithm for `fmincon` is the fastest one and that it is also able to find the global minimum. `sqp` was therefore selected as the optimization algorithm which is used by `fmincon` to find a local minimum.

Chapter 4

Verification of the optimization routine

In this chapter, it will be verified whether or not the optimization routine behaves correctly. Furthermore, a comparison will be made between different mesh sizes and different configurations of the control points for the Bézier surface. The best mesh size and control point configuration will then be used to generate the body force field for several voltage amplitudes and frequencies in chapter 5.

4.1 Observed order of the *icoFoamBF* solver

In order to perform a verification on the *icoFoamBF* solver, use was made of a Richardson extrapolation [43], which is based on a series expansion of the discretisation error as displayed in equation (4.1):

$$\varepsilon = \mathbf{u} - \mathbf{u}_{exact} = g_1 h + g_2 h^2 + g_3 h^3 + g_4 h^4 + \mathrm{HOT} \tag{4.1}$$

In the equation, h is the grid spacing, g_i are the coefficients for ith order error term and HOT are the higher order terms.

For a solution with a fine mesh (spacing h_1) and a coarser mesh (spacing h_2), the following equations hold:

$$\mathbf{u}_1 = \mathbf{u}_{exact} + g_{\widehat{p}} {h_1}^{\widehat{p}} + \mathrm{HOT} \tag{4.2}$$

$$\mathbf{u}_2 = \mathbf{u}_{exact} + g_{\widehat{p}} {h_2}^{\widehat{p}} + \mathrm{HOT} \tag{4.3}$$

Table 4.1: Different meshes, their characteristics and needed computation time for 1 iteration. Note that the computation time is just a rough indication, as test conditions (such as CPU load) where not equal for all meshes.

mesh name	number of cells	normalized cell spacing	computation time
coarse	12400	2	303 min
medium-coarse	17856	1.67	640 min
medium	24304	1.43	1765 min
medium-fine	31744	1.25	2248 min
fine	40176	1.11	2096 min
superfine	49600	1	3549 min

The ratio between the mesh spacings is now defined as $r = h_2/h_1$. The exact solution can subsequently be calculated according to equation (4.4):

$$\mathbf{u}_{exact} = \mathbf{u}_1 + \frac{\mathbf{u}_1 - \mathbf{u}_2}{r^{\widehat{p}} - 1} \tag{4.4}$$

In table 4.1, a number of meshes are summarized that have been used for the calculation of the exact solution and the observed order of the numerical scheme.

An estimation of the exact solution, $\mathbf{u}_{exact}$, was calculated for all possible combinations of these meshes, with $\mathbf{u}_1$ always being calculated with a finer mesh than $\mathbf{u}_2$. This gives $5+4+3+2+1 = 15$ different solutions for $\mathbf{u}_{exact}$. The final value for $\mathbf{u}_{exact}$ was chosen to be the mean of these 15 different solutions.

Now that $\mathbf{u}_{exact}$ is calculated, the discretisation error for the six different meshes can be computed. Two different measures for the global norm of the discretisation error were computed, as suggested by Roy [46]. These two measures are defined according the equation (4.5) and (4.6).

$$L_\infty = \max \mid \mathbf{u} - \mathbf{u}_{exact} \mid \tag{4.5}$$

$$L_2 = \sqrt{\frac{\sum_{n=1}^{N} \mid \mathbf{u} - \mathbf{u}_{exact} \mid^2}{N}} \tag{4.6}$$

These two global norms were computed for all of the six meshes given in table 4.1 and the distribution of the global norms can be seen in figure 4.1. A power law fit was also calculated for the two global norms, which showed an observed order of $\widehat{p} = 1.03$ for the L_∞-norm and $\widehat{p} = 1.05$ for the L_2-norm. For convenience, also the lines showing first order and second order accuracy are displayed in the figure.

According to Roy [46], testing whether the observed order of accuracy matches the formal order of accuracy is "the most rigorous code verification test" [46, p.134] and thus the recommended test to check whether the code behaves as it is expected and whether the discretisation error is reduced at approximately the same rate as the formal order of accuracy prescribes. Since the formal order of an upwind discretisation scheme is 1, the observed order

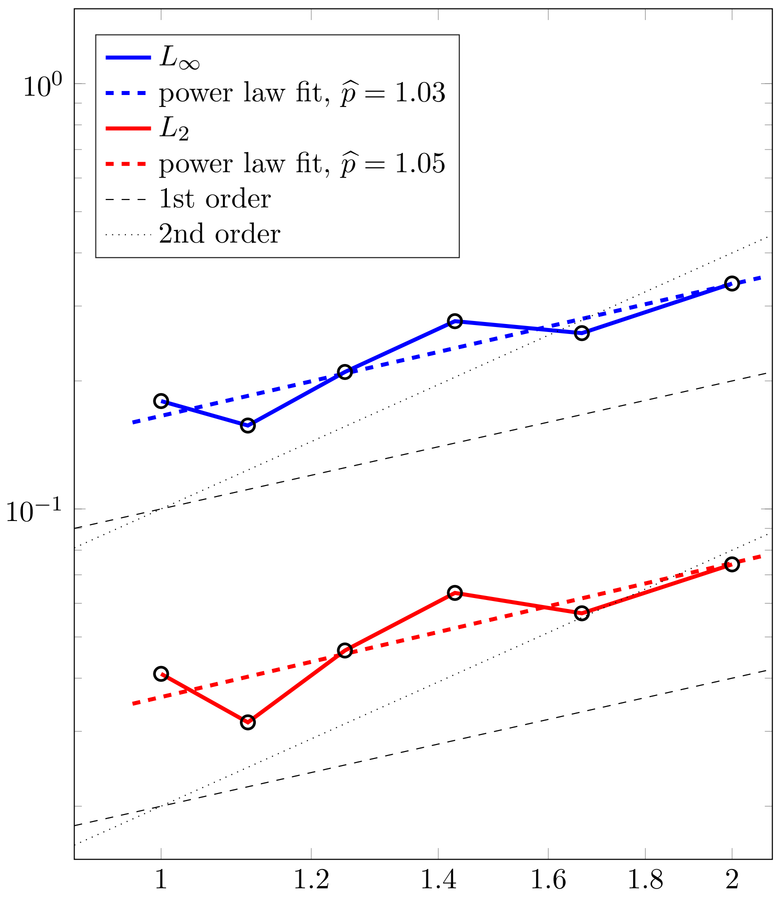

Figure 4.1: Global norms for the discretisation error for different normalized cell spacings, together with a power law fit to find a value for the observed order of the numerical scheme. 1st order and 2nd order slopes are plotted in black. The global norms follow the 1st order slope, which is expected since an upwind scheme is used.

of accuracy can be said to match the formal order of accuracy closely and it can be concluded that the *icoFoamBF* solver behaves correctly.

4.2 Analysis and optimization of the mesh

To improve the results of the optimization routine, an in-depth investigation of the mesh was performed. First, an assessment was made of the influence of numerical dissipation in section 4.2.1. After that, different configurations of the mesh were tested and compared to the meshes used to calculate the observed order of the *icoFoamBF* solver (see section 4.1). This is done using independent coordinate refinement in the x- and y-direction. The results of this analysis can be found in section 4.2.2. The best mesh is then chosen and an assessment of the influence of numerical dissipation is performed again for this chosen mesh in section 4.2.3.

4.2.1 The effect of numerical dissipation

A quick assessment was made of the influence of numerical dissipation resulting from using an upwind discretisation scheme. According to Raithby [42], there are three conditions which must hold for an upwind discretisation to yield accurate results:

- Only very small frequencies are allowed if transients are present.
- If applicable, the source term must be nearly uniform throughout the grid.
- The grid Peclet number should be higher than 10 or lower than 0.2 in the presence of diffusion.

Since a steady-state solution is calculated, transients are not present and the first condition is fulfilled. The second condition states that the source term must be nearly uniform across the grid. Since the body force field covers only a very small part of the grid, it can be argued that the source term is indeed nearly uniform across the grid since it is equal to zero almost everywhere. Of course, in the region where the body force is applied, the source term is far from uniform and thus the second condition is probably not fulfilled.

For evaluating the third condition, the Peclet number was calculated for both the coarse and the superfine mesh. A distribution of the Peclet numbers is displayed in figure 4.2. As can be seen in the figure, the Peclet number is very unlikely to be higher than 10 for both the coarse mesh and the superfine mesh. Some parts of the grid however have a Peclet number which is smaller than 0.2, and in the case of the superfine mesh the Peclet number is smaller than 1 in most parts of the mesh. Raithby [42, p.86] calculated that a Peclet number of 2 is the most undesirable and that a Peclet number of 1 results in an error of approximately 10%. The superfine mesh should thus keep the error limited, while the coarse mesh will produce a larger error due to the higher Peclet numbers.

A refinement of the mesh thus reduces the influence of numerical dissipation, but it can also be reduced by using a higher-order scheme. Since using an higher-order scheme results in stability problems however, the only option to reduce numerical dissipation in this case is

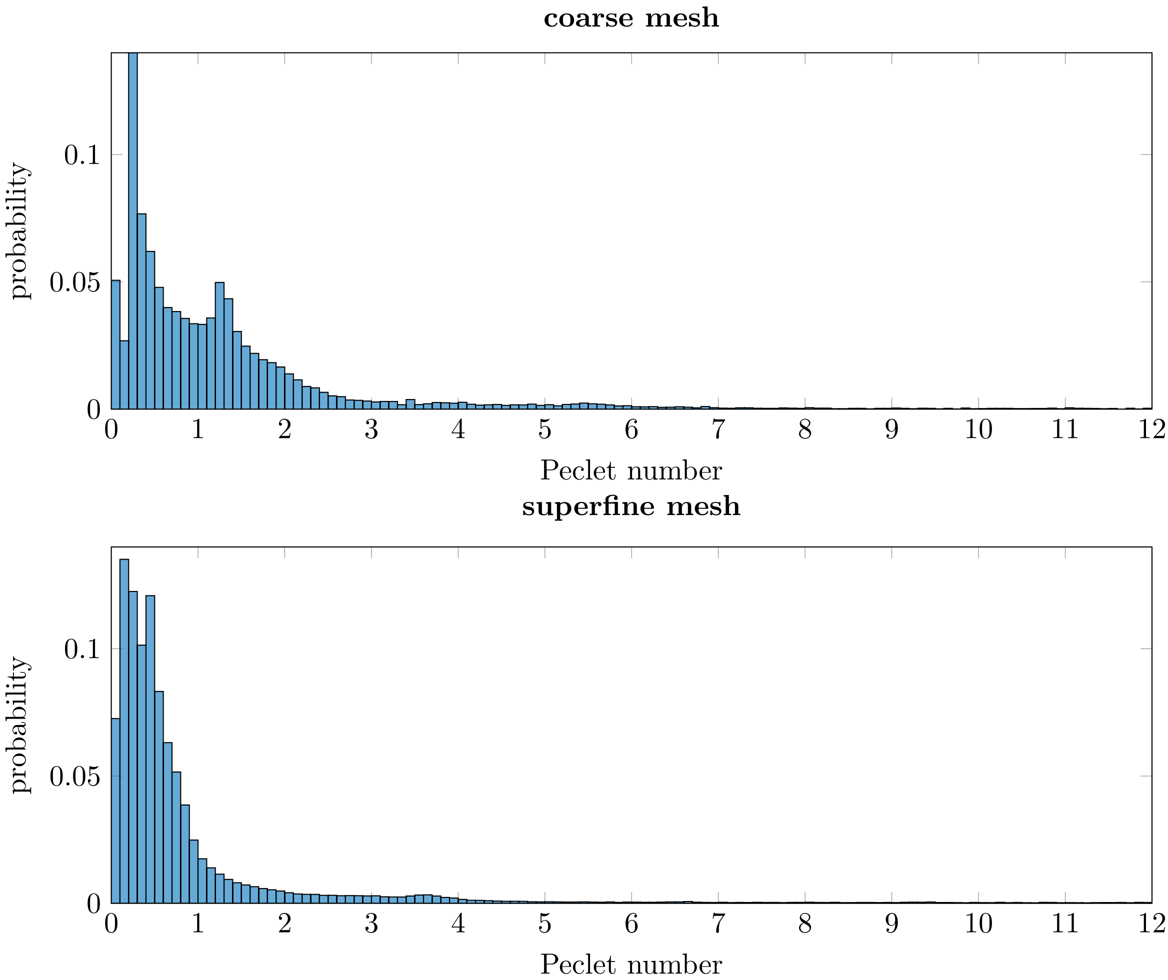

Figure 4.2: Probability density distribution of the Peclet number for the coarse mesh and the superfine mesh.

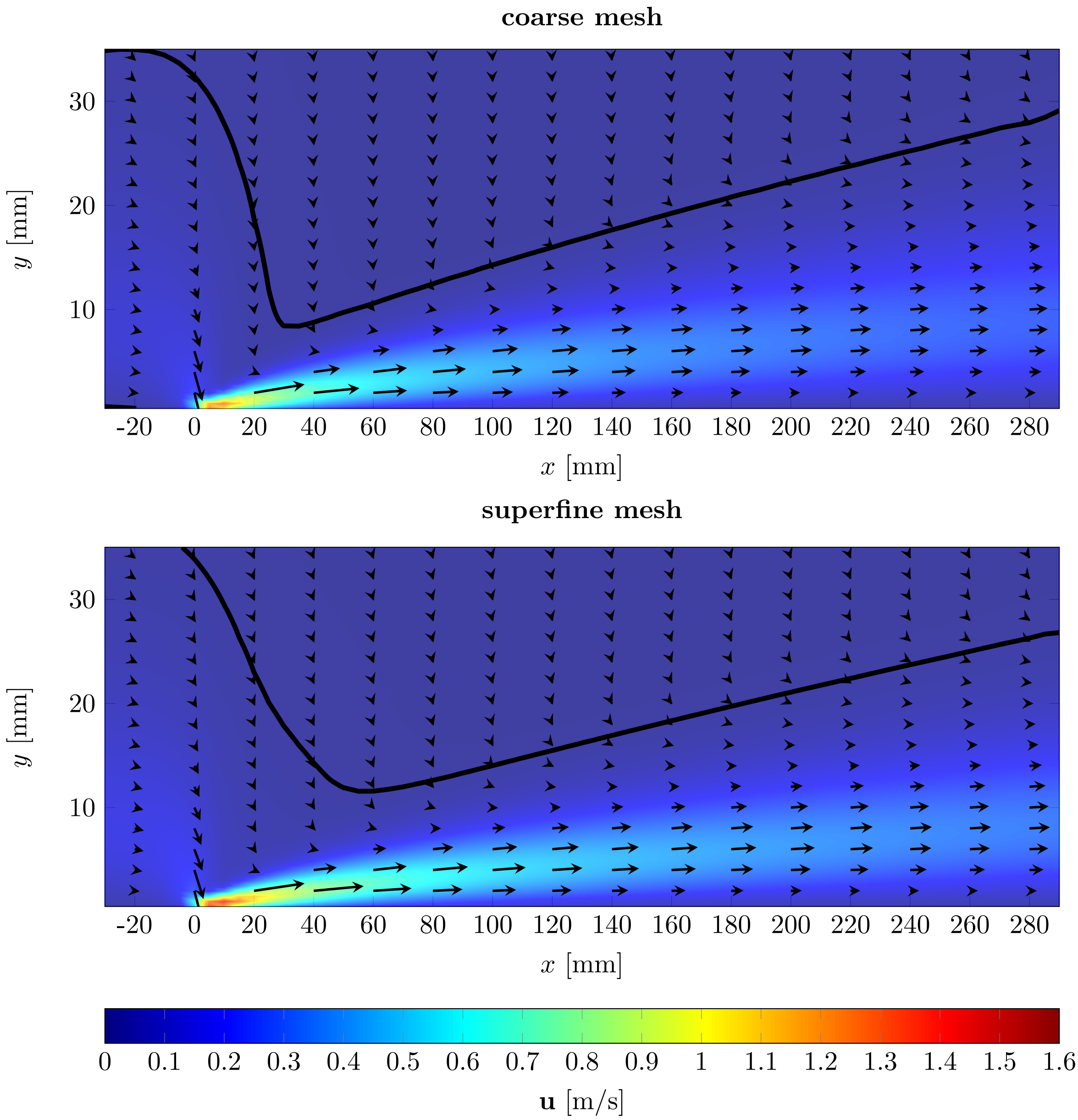

Figure 4.3: Converged flow fields for both the coarse mesh and the superfine mesh. The black contour indicates where the velocity is equal to 0.2 m/s. It is clear that both the maximum velocity and the area where the velocity is higher than 0.2 m/s are larger for the superfine mesh. Furthermore, the produced jet stays confined within a slightly thinner layer in the case of the superfine mesh.

Table 4.2: Mesh refinement in x- and y-direction.

mesh	number of cells	L_∞	L_2
coarse	12400	0.349	0.075
x-refinement	24800	0.299	0.072
y-refinement	24800	0.225	0.043

to refine the mesh. Figure 4.3 shows the converged flow field for the coarse mesh and the superfine mesh as defined in table 4.1.

It is clear that numerical dissipation is significant when comparing the coarse mesh with the superfine mesh. Both maximum and mean velocities are higher for the superfine mesh, while the produced jet is 'spread out' over a larger area in the case of the coarse mesh.

4.2.2 Independent coordinate refinement of the mesh

In order to try to improve the mesh, a refinement of the mesh was made in x- and y-direction separately. The coarse mesh (see table 4.1) was used as a basis, in which the number of cells in x-direction and the number of cells in y-direction were doubled respectively. To assess the quality of the mesh, the global norms defined in equations (4.5) and (4.6) and the exact solution computed in section 4.1 were used here as well. The results can be seen in table 4.2.

It is clear from table 4.2 that a refinement in y-direction is the most effective. However, the number of cells in the mesh is now doubled, while it should be kept as low as possible to reduce the computation time. Therefore, different configurations of the mesh were evaluated which all had fewer or as much cells as the coarse mesh and entailed a refinement of the mesh in y-direction but a coarsening of the mesh in x-direction. In order to quantify the refinement and coarsening of the mesh, following definitions were used:

$$\mathrm{r}_x = \frac{\Delta x_{\text{coarse}}}{\Delta x} = \frac{\mathrm{n}_x}{\mathrm{n}_{x\text{coarse}}} \tag{4.7}$$

$$\mathrm{r}_y = \frac{\Delta y_{\text{coarse}}}{\Delta y} = \frac{\mathrm{n}_y}{\mathrm{n}_{y\text{coarse}}} \tag{4.8}$$

where r_x and r_y are the refinement ratios in x- and y-direction respectively and n_x and n_y are the number of cells in x- and y-direction respectively. The configurations of the mesh that were constructed and tested are displayed in table 4.3, together with their global norms and the maximum and mean velocities.

Configuration 1 uses a very coarse mesh in x-direction and a very fine mesh in y-direction, but the global norms are much too large and this mesh is thus disregarded. The second configuration consists of the same number of cells is the first configuration, but the number of cells in x-direction is doubled and the number of cells in y-direction is halved with respect to the first configuration. The global norms are already smaller compared to the coarse mesh, but it can be improved even more by further increasing the number of cells in y-direction and reducing the number of cells in x-direction. Configuration 3 and configuration 4 both

Table 4.3: Improving the coarse mesh using grid refinement in y-direction and grid coarsening in x-direction.

mesh	number of cells	r_x	r_y	L_∞	L_2	$\mathbf{u}_{max}$ [m/s]	$\mathbf{u}_{mean}$ [m/s]
coarse	12400	1	1	0.349	0.075	1.440	0.096
superfine	49600	2	2	0.184	0.041	1.566	0.110
config. 1	11904	0.4	2.4	2.439	1.077	2.589	0.807
config. 2	11904	0.8	1.2	0.307	0.060	1.454	0.104
config. 3	8928	0.6	1.2	0.284	0.049	1.505	0.111
config. 4	10416	0.6	1.4	0.299	0.054	1.496	0.112

Table 4.4: Parameters of the final mesh.

number of cells	cells in x-direction	cells in y-direction
8928	93	96

use a cell refinement in x-direction of 0.6, meaning that the number of cells in x-direction is reduced by 40% compared to the coarse mesh. Configuration 3 and configuration 4 increase the number of cells in y-direction with 20% and 40% respectively. For both configurations, the global norms are reduced even further than was the case for the second configuration. Surprisingly, the coarser mesh of configuration 3 performs better than configuration 4. Since the number of cells in configuration 3 is only 8928, the optimization can be performed much faster and therefore this configuration is chosen as the final choice for the mesh.

4.2.3 Final mesh choice

As was determined in the previous section, the final mesh is defined by the parameters given in table 4.4 and is displayed in figure 4.4.

To perform a final check whether the chosen mesh will yield accurate results, again the Peclet numbers and the velocity field are calculated and compared to the coarse and the superfine mesh in figure 4.5 and 4.6 respectively.

Looking at the Peclet number distributions in figure 4.5, the distribution resulting from the chosen mesh (config. 3) is already much better than the coarse mesh and very similar to the superfine mesh. The majority of the Peclet numbers is smaller than 1, suggesting that the error will not exceed 10% in most places. Comparing the velocity field of the final mesh with the coarse and the superfine mesh in figure 4.6, it is immediately clear that the region where the velocity is higher than 0.2 m/s is larger for the final mesh than for the other meshes and that this region more closely resembles the one from the superfine mesh than from the coarse mesh. Also, the maximum velocity is higher in the final mesh than it is in the coarse mesh (see table 4.3), suggesting that the influence of numerical dissipation is lower in the final mesh than in the coarse mesh while also lowering the number of cells and speeding up the optimization routine.

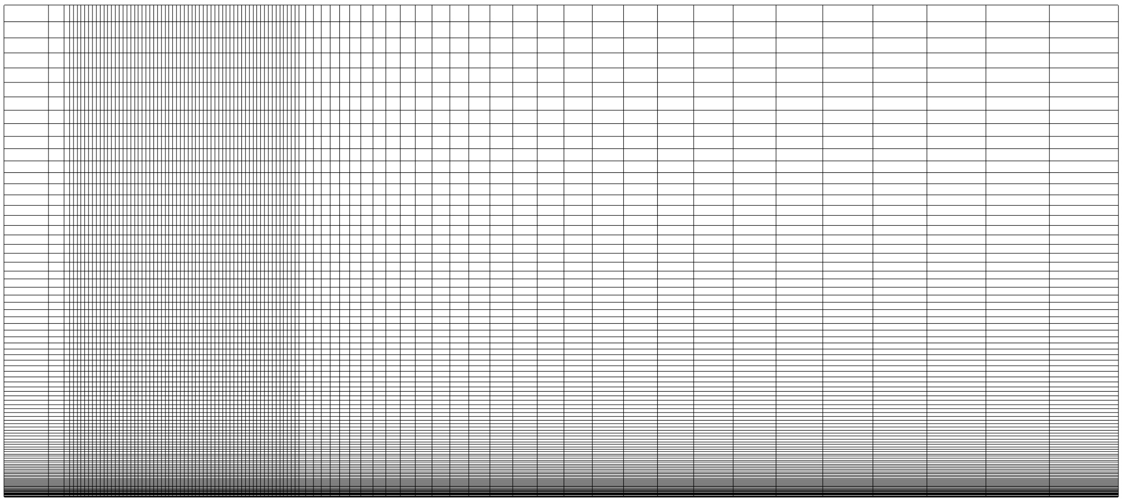

Figure 4.4: Layout of the final mesh.

4.3 Analysis and optimization of the parametrization of the body force field

As explained in chapter 3, the body force field will be represented by a parametrized surface in order to drastically reduce the number of variables and to increase the speed at which the optimization of the body force field is performed. It was chosen to parametrize the body force field by using a Bézier surface, using $n \times m$ internal points. Since both the force in x- and in y-direction needs to be optimized, the number of variables in the optimization is equal to $2(n \times m)$. The higher the number of internal control points, the better the representation of the surface will be. On the other hand, increasing the number of control points also increases the number of variables for the optimization. To increase the chance that a global minimum will be found, the number of starting points for the `MultiStart` algorithm should be increased when more control points are used.

If there is for example only one control point, there are two variables that need to be optimized: a variable that determines the body force in the x-direction and a variable that determines the body force in the y-direction. When it is desired to generate starting points such that each variable can assume four different values within some bounds, there are $4^2 = 16$ different starting points which need to be analysed by the algorithm. This is illustrated in figure 4.7. If there are $2 \times 2 = 4$ internal points and thus 8 variables for the optimization routine, and each variable can assume again 4 different values, there are already $4^8 = 65536$ different combinations and thus starting points that need to be ran. This will of course take way too much time, and therefore the number of starting points will be fixed at 50, from which only the starting points are taken which satisfy the following condition:

- The net body force in x-direction must be positive (pointing to the right).

To find the optimal number and layout of internal control points, the Bézier surface was optimized directly using the same `MultiStart` optimization routine as is used for the opti-

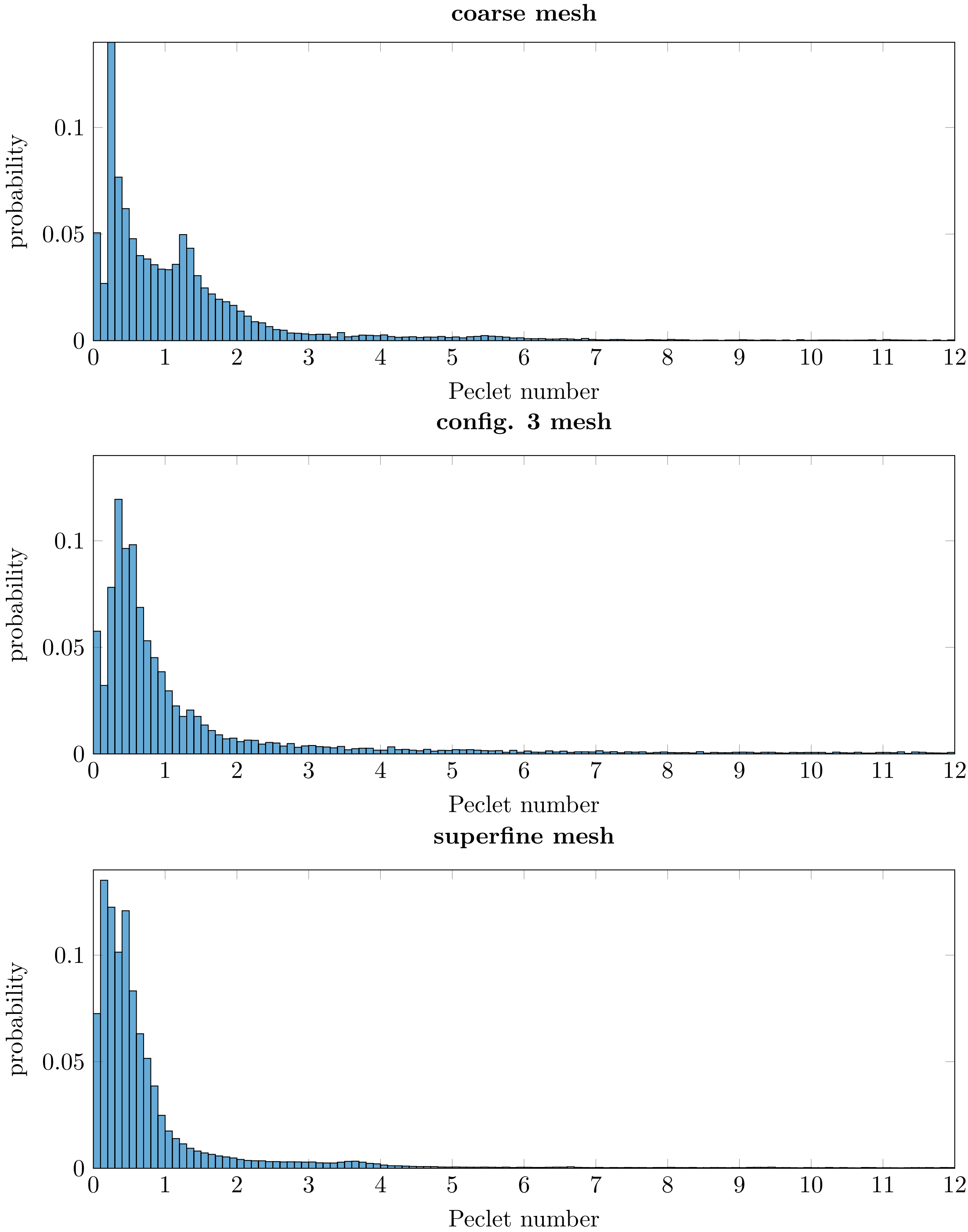

Figure 4.5: Probability density distribution of the Peclet number for the coarse mesh, the final mesh (config. 3) and the superfine mesh.

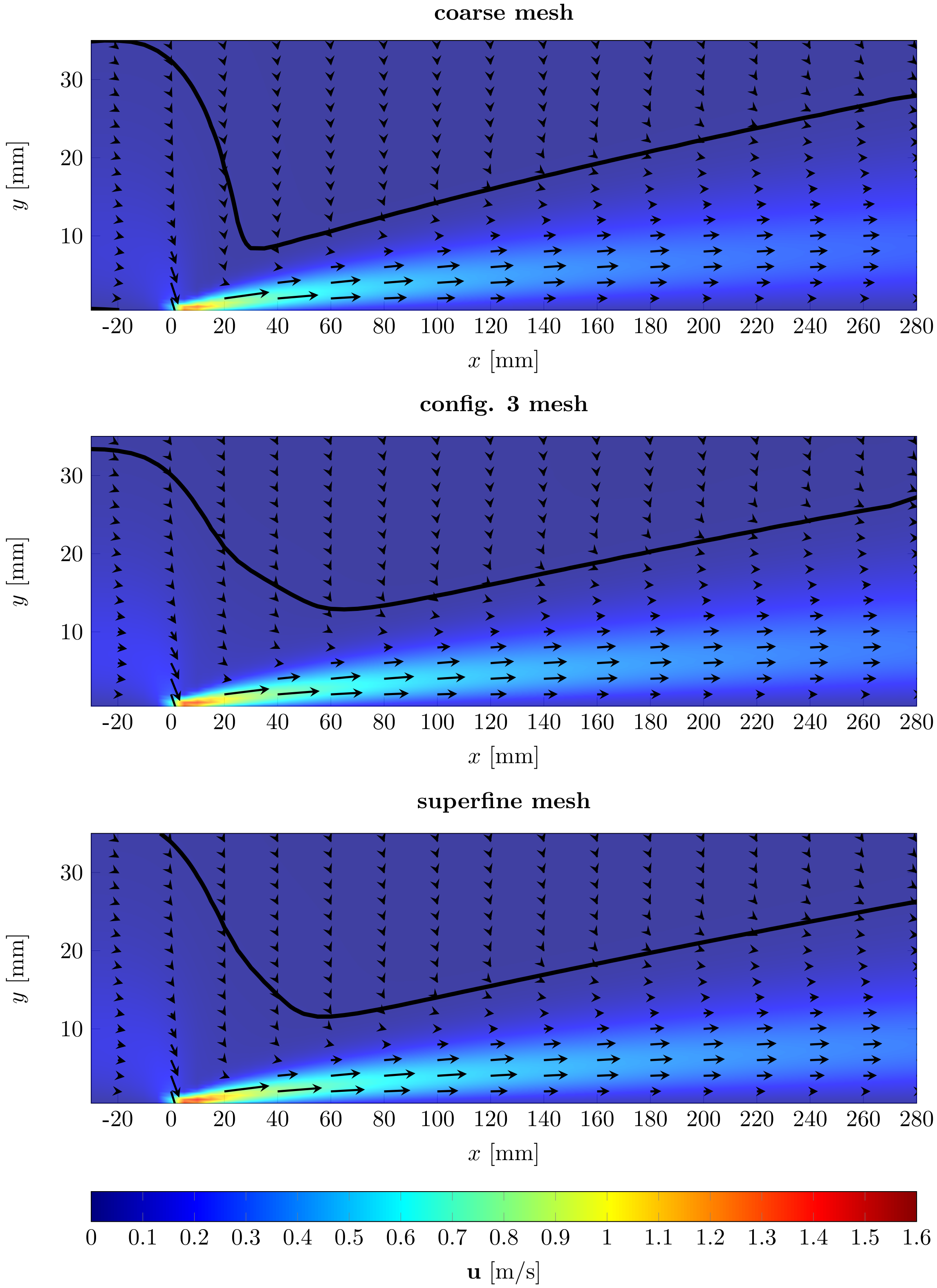

Figure 4.6: Converged flow fields for the coarse mesh, the final mesh (config. 3) and the superfine mesh. The black contour indicates where the velocity is equal to 0.2 m/s.

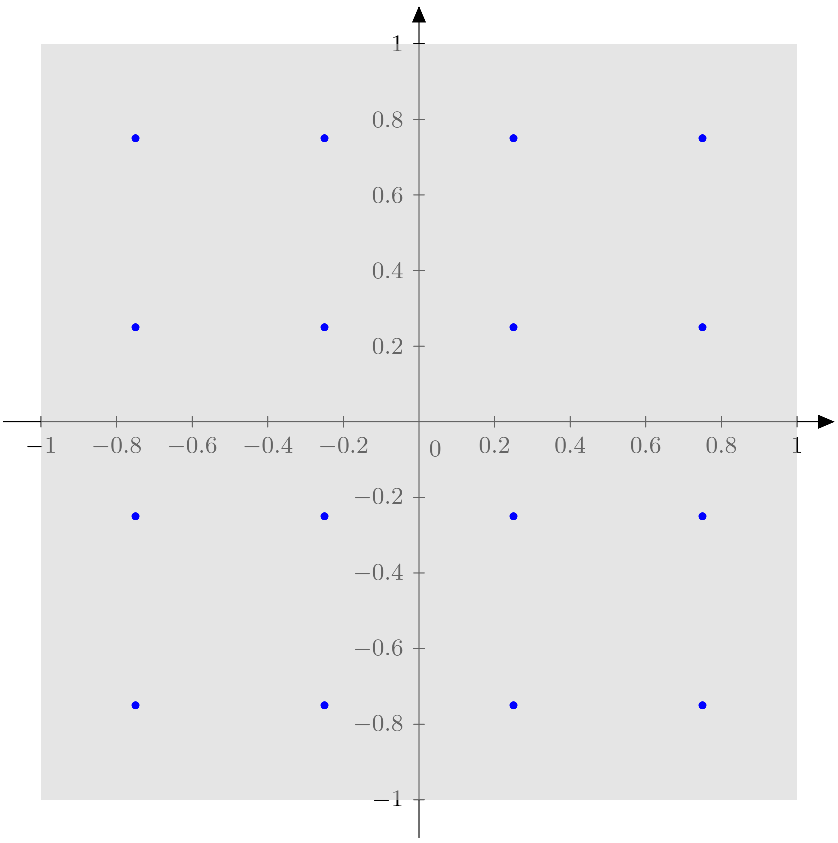

Figure 4.7: Starting points for the `MultiStart` optimization algorithm for a 1×1 grid of internal control points and 4 different values that each variable can assume.

Table 4.5: Different configurations for the internal control points.

configuration	residual	function evaluations
1×2	95.19	6263
2×1	96.42	5345
2×2	92.92	9884
2×3	89.47	21200
2×4	95.03	30407
3×2	82.66	22711
3×3	95.20	25934
4×2	90.03	23693
5×2	89.19	34030

mization of the body force field. The reference body force field is extracted from a velocity field using the hybrid method proposed by Kotsonis et al [30]. By optimizing the Bézier surface directly using an actual possible body force field as reference, the ability of different control point configurations to represent an actual body force field could be investigated.

An illustration of the effectiveness of different configurations for the internal control points is given in figure 4.8, while table 4.5 gives an overview of how close each configuration gets to the reference body force field and how many function evaluations were needed to complete the optimization.

Looking at figure 4.8, it can be seen that none of the configurations for the internal control points is able to replicate the swirling behaviour of the reference body force field except for the 3×2 configuration. In order to get better resemblance between the optimized body force fields and the reference field, an extra constraint was imposed on the net force, this time in the y-direction. To find out whether the force in y-direction needed to be contrained as positive or as negative, both constraints were tried for the 3×2 configuration. The resulting optimized body force fields can be found in figure 4.9.

It can be seen that when constraining the net force in y-direction to be positive, the resulting body force field does not resemble that reference field at all. When constraining the net force in y-direction to be negative however, the body force field resembles both the reference field and the optimized body force field with no restrictions on the force in y-direction. Looking at the residuals, constraining the net force in y-direction is actually beneficial and results in a lower residual than not constraining it. Therefore it was chosen to add an additional constraint to the body force field such that following conditions must now hold:

- The net body force in x-direction must be positive (pointing to the right).
- The net body force in y-direction must be negative (pointing downward).

With the body force field being constrained by above conditions, the effectiveness of different configurations for the internal control points was again investigated. An illustration can be found in figure 4.10, while the results are summarized in table 4.6.

It can be seen from figure 4.10 that now four configurations are able to replicate the swirling form of the reference field: the 3×2 configuration, the 4×2 configuration, the 5×2

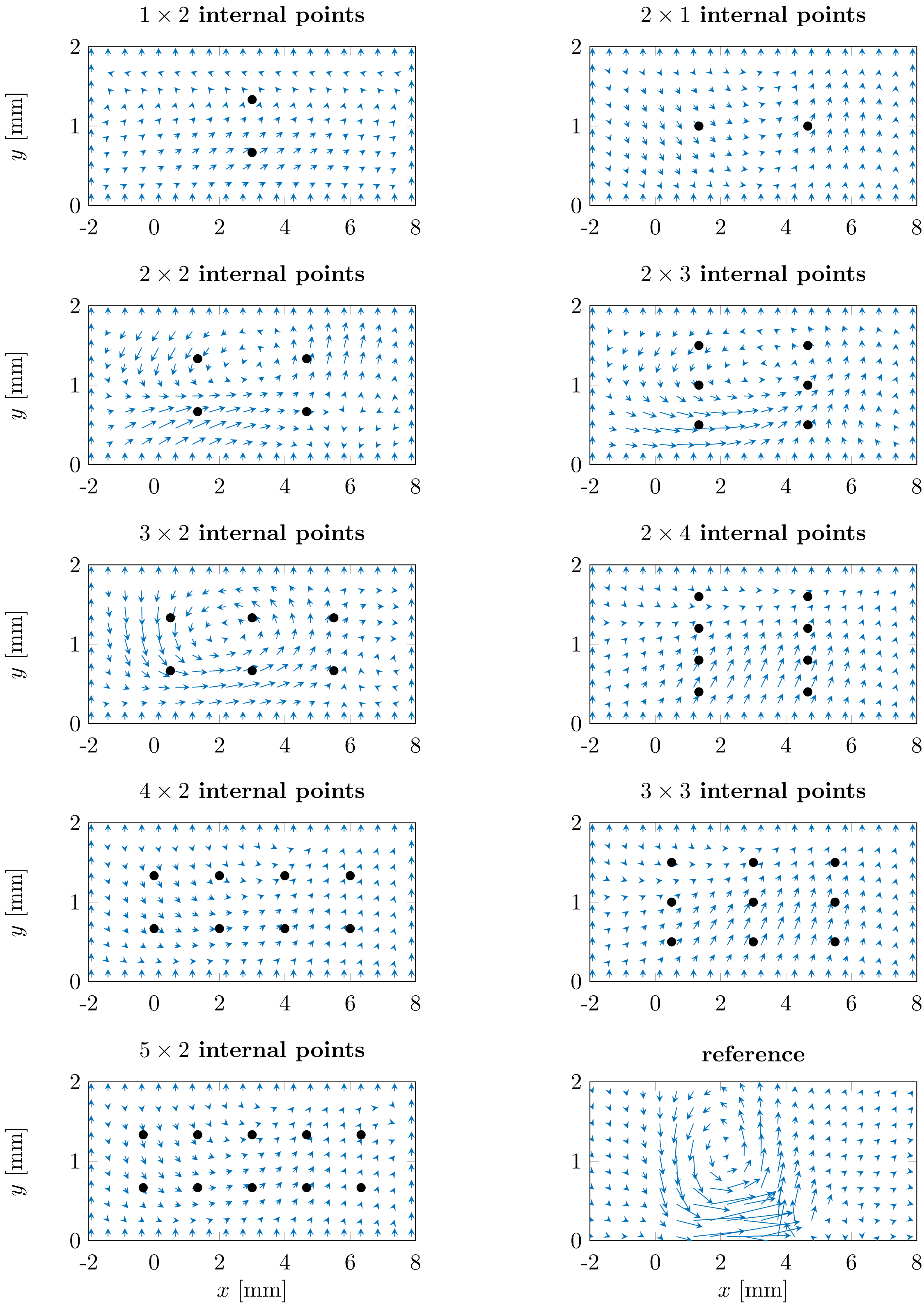

Figure 4.8: Different configurations of the internal control points and their effectiveness to approximate a given body force field.

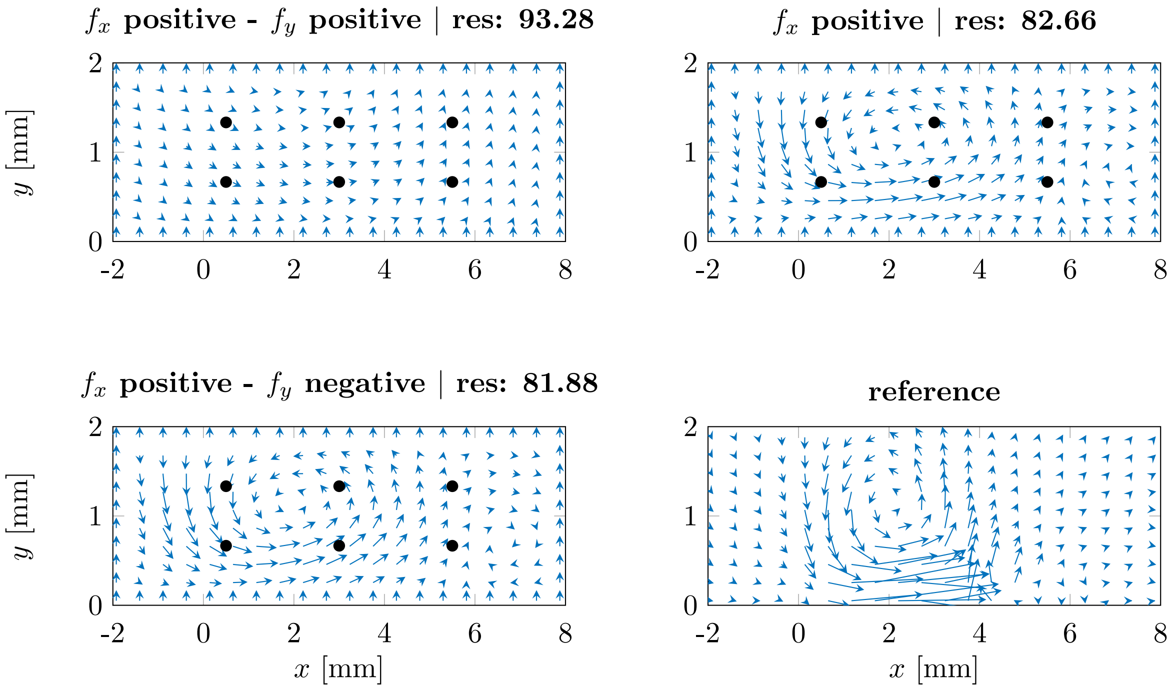

Figure 4.9: Effect of constraints on net force in y-direction on opimized body force field.

Table 4.6: Different configurations for the internal control points with an additional constraint on the net force in y-direction.

configuration	residual	function evaluations
1×2	95.99	3175
2×1	96.16	2129
2×2	86.05	8551
2×3	84.86	8901
2×4	87.38	14547
3×2	81.88	9528
3×3	84.24	24533
4×2	79.07	21351
5×2	73.44	24164

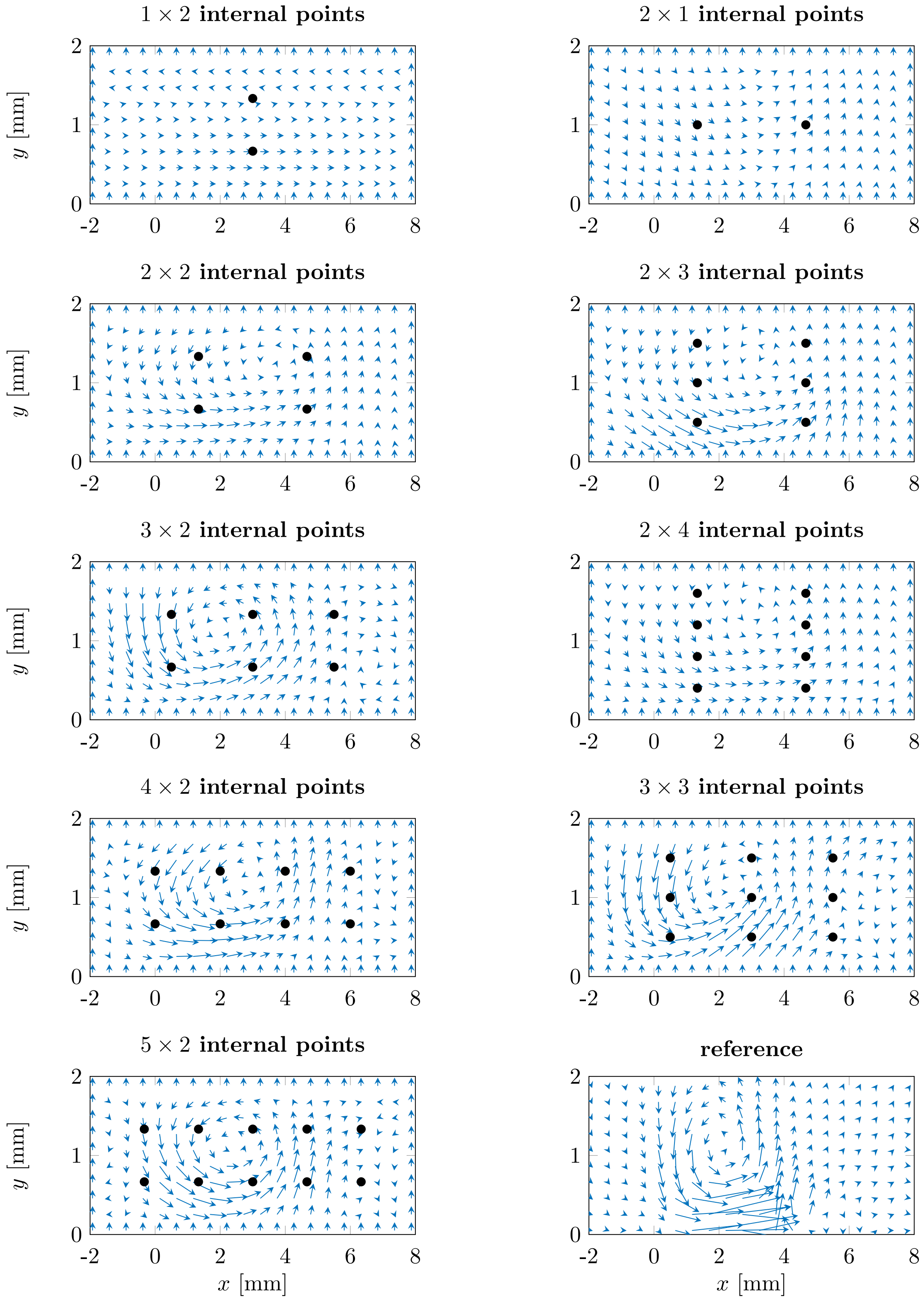

Figure 4.10: Different configurations of the internal control points and their effectiveness to approximate a given body force field with an additional constraint on the net force in y-direction.

configuration and the 3×3 configuration. Looking at table 4.6, it can be seen that 5×2 internal control points clearly performs the best but needs 24164 function evaluations in order to complete the optimization. 3×2 internal control points requires far less function evaluations, which will shorten the computation time for optimizing the body force field but will still result in a reasonably small residual. It must however be pointed out that none of the configurations were able to replicate the large forces visible at the bottom of the reference field. This is because of the parametrization of the body force field, which implicates that peaks in the body force field will always be smoothed out. However, one must also consider the possibility that the large forces at the bottom of the reference field are non-physical and due to experimental errors. The reference force field is namely derived from a velocity field which was obtained using PIV measurements. Near the wall though, PIV measurements are known to have a higher uncertainty due to a number of factors including a large velocity gradient and wall reflections [27]. The body force near the wall may thus not be as large as shown in the reference field.

Chapter 5

Results

The optimization of the body force field was performed for 8 different cases, which are summarized in table 5.1. The cases include 5 different values for the peak-to-peak voltage amplitude and 4 different values for the voltage frequency. This chapter will first present the integral values of the body force for each case, after which the computed velocity field will be compared to the benchmark velocity field to see whether the optimization routine was able to approach the benchmark solution sufficiently or not. Lastly the body force fields will be displayed together with the pressure gradients and an analysis will be made of the influence of the pressure gradient compared to the body force.

5.1 Integral body forces

The body force was integrated over the entire body force field to calculate the integral value of the body force exerted on the fluid. Figure 5.1 presents the integral body force in x- and y-direction for 5 different voltage amplitudes, while figure 5.2 displays the integral body force for 4 different voltage frequencies.

Table 5.1: Cases for which the body force field was optimized.

case number	voltage amplitude	voltage frequency
case 1	8 kV	2 kHz
case 2	10 kV	2 kHz
case 3	12 kV	2 kHz
case 4	14 kV	2 kHz
case 5	16 kV	2 kHz
case 6	10 kV	1 kHz
case 7	10 kV	3 kHz
case 8	10 kV	4 kHz

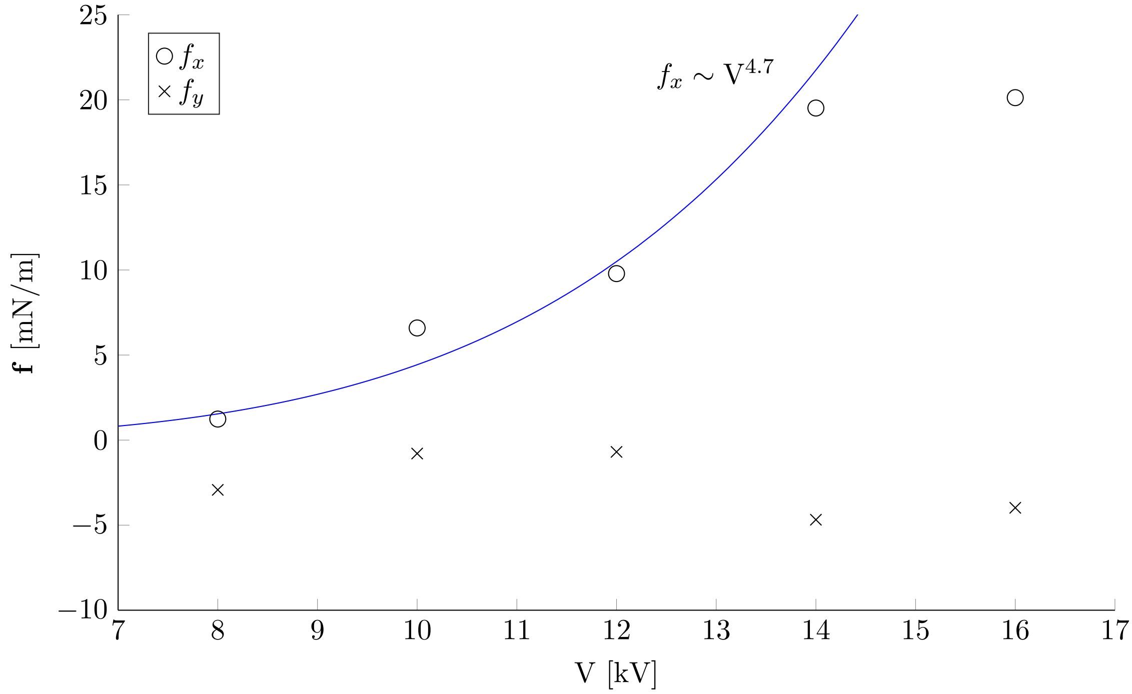

Figure 5.1: Integral body force in x- and y-direction for different voltage amplitudes and a voltage frequency of 2 kHz.

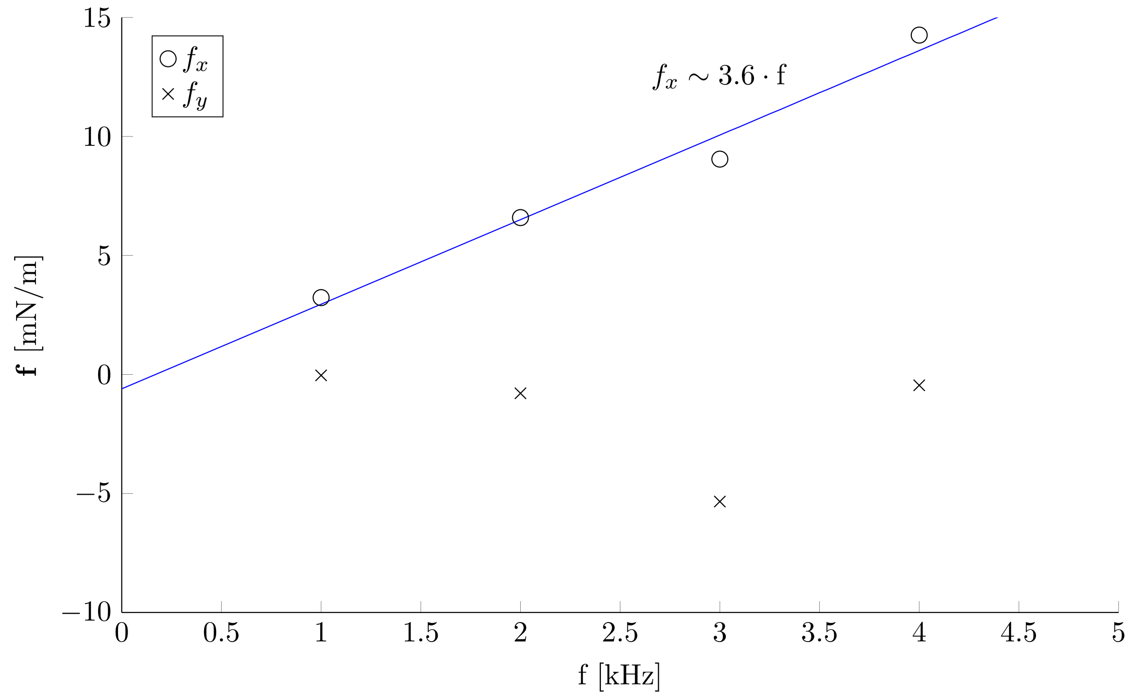

Figure 5.2: Integral body force in x- and y-direction for different voltage frequencies and a voltage amplitude of 10 kV.

It can be seen in figure 5.1 that the body force in x-direction increases with voltage amplitude more or less according to a power law with $f_x \sim \mathrm{V}^{4.7}$, except for the case where the voltage amplitude is 16 kV. This could be due to the fact that the bounds between which the Bernstein coefficients were defined were not taken large enough, or it could also be the case that the global minimum was not found during the optimization procedure. However, the fact that the force in x-direction increases with voltage amplitude according to a power law for the first 4 cases has previously also been found by Abe et al [1], Thomas et al [56] and Kotsonis et al [30]. The force in y-direction stays rather small for all voltages, but no clear trend can be observed which clarifies whether f_y increases or decreases with increasing voltage amplitude.

Looking at figure 5.2, the body force in x-direction seems to increase with increasing voltage frequency more or less linearly, with $f_x \sim 3.6 \cdot \mathrm{f}$. Also Abe et al [1] and Kotsonis et al [30] found the thrust in x-direction to increase linearly with voltage frequency. The body force in y-direction again does not show a clear trend but stays rather small except for a voltage frequency of 3 kHz. This is probably due to the fact that the minimum for 3 kHz was found starting from another initial point than the other voltages frequencies. This will be further explained in section 5.3.

5.2 Comparison between calculated and benchmark velocity field

To give an idea of how close the optimized velocity field matches the benchmark flow field, the maximum velocities in x-direction are compared as well as the minimum (or maximum negative) velocities in y-direction in figure 5.3 for the different voltage amplitudes and figure 5.4 for the different voltage frequencies respectively.

It can be seen that the minimum velocities in y-direction resulting from the optimized body force field match those from the benchmark data quite closely for both the different voltage amplitudes and voltage frequencies. Only for a voltage amplitude of 10 kV and a voltage frequency of 2 kHz (both are actually the same case, namely case 2), the computed minimum velocity in y-direction is lower than the benchmark. For the maximum velocities in x-direction there is equally a close match except for a voltage amplitude of 16 kV and to a lesser extent again for case 2. The difference between the calculated velocity and the velocity from the experiment is quite large for the case where the voltage amplitude is 16 kV, suggesting indeed that the global minimum has not been found or even approached. This would then explain why the integral body force in x-direction for a voltage amplitude of 16 kV does not follow the trend in figure 5.1.

Comparing maximum and minimum velocities might however not be representative for the resemblance between the calculated velocity field and the benchmark velocity field. Therefore, in order to obtain a clearer understanding of how closely the velocity field resulting from the optimized body force field matches the velocity field used as benchmark, both velocity fields are plotted for case number 2 (see table 5.1). The velocity fields are plotted in figure 5.5 as well as the difference between the two fields which is defined as the benchmark field minus the optimized field. Furthermore, velocity profiles at several streamwise locations are displayed in figure 5.6.

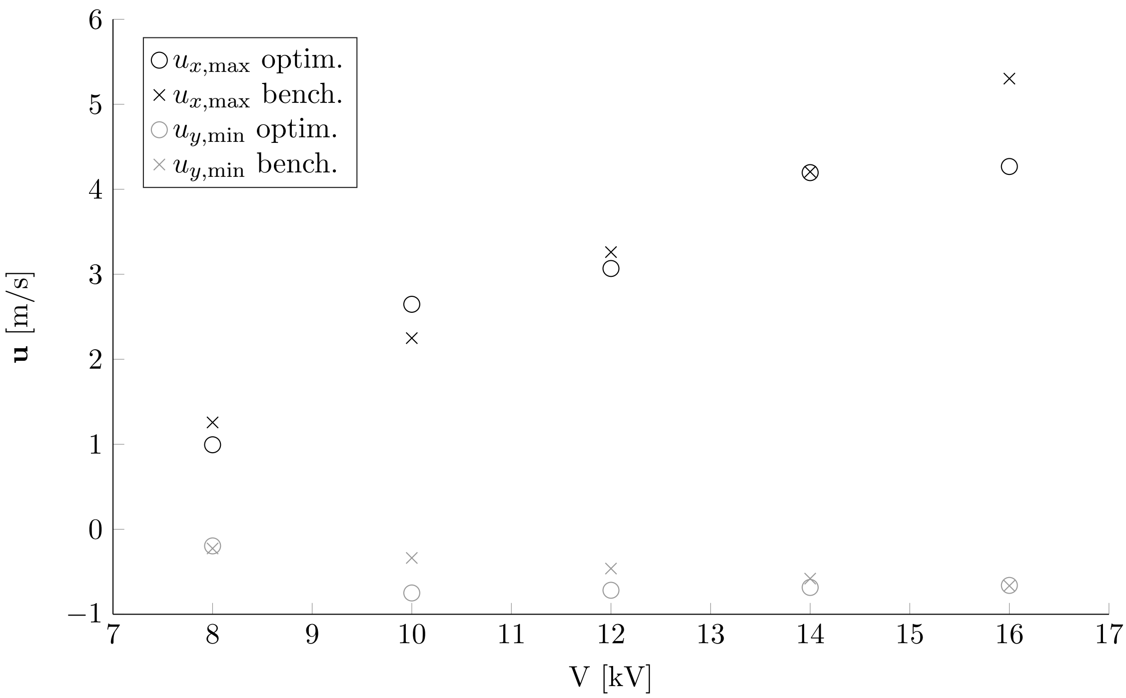

Figure 5.3: Maximum velocity in x-direction and minimum velocity in y-direction for different voltage amplitudes and a voltage frequency of 2 kHz.

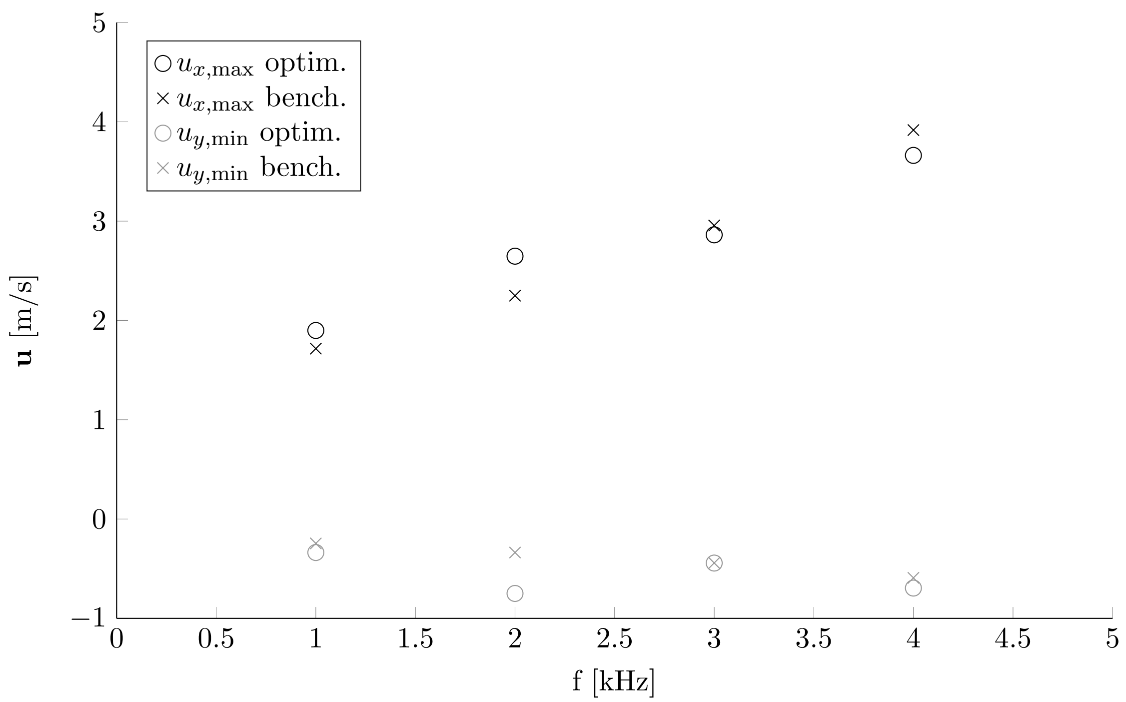

Figure 5.4: Maximum velocity in x-direction and minimum velocity in y-direction for different voltage frequencies and a voltage amplitude of 10 kV.

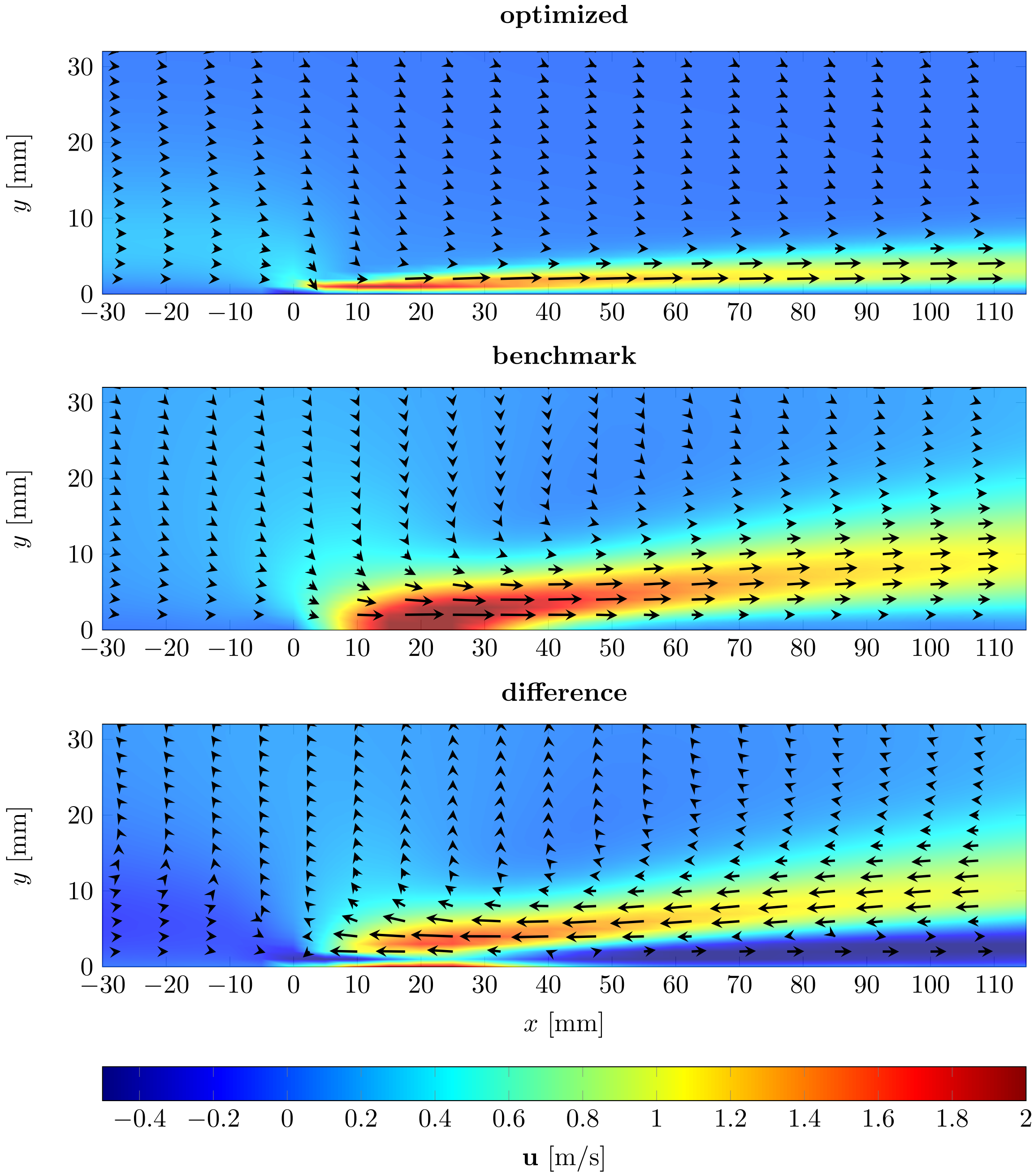

Figure 5.5: Velocity field obtained from the optimized body force field, the benchmark velocity field and the difference between them.

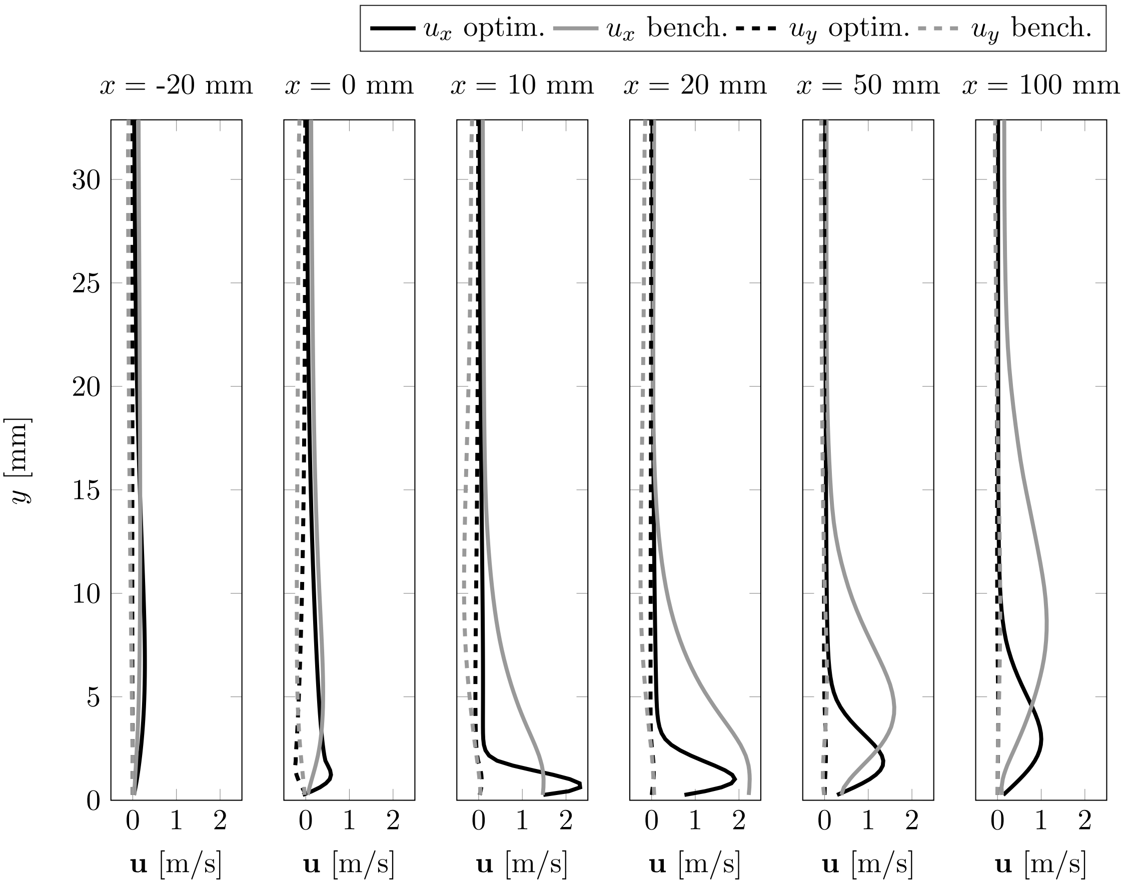

Figure 5.6: Velocity profiles obtained from the optimized body force field together with the benchmark velocity profiles.

Comparing the velocity field obtained from the optimized body force field with the benchmark velocity field in figure 5.5, it can immediately be seen that the jet in the optimized field is much thinner than the one from the benchmark. This is probably due to the fact that the body force field is defined on a very small region (from -2 to 8 mm in x-direction and from 0 to 2 mm in y-direction). Furthermore, the optimized velocity field is zero at the plate, which is not the case in the benchmark field. This is due to the fact that the Bézier surface was defined to be zero at the edges and thus also at the plate, which explains why the velocity is zero at the plate in the optimized case. Looking at the difference between the two velocity fields (defined as the benchmark field minus the optimized field), the velocities are higher were the optimized jet is present, whereas the velocities are lower were the optimized jet is not present. The optimization procedure thus tried to compensate for the fact that the optimized jet is much thinner than the benchmark jet by increasing the velocity in the optimized jet to achieve a lower mean difference. If the maximum difference would be used as optimization objective instead of the mean difference, the two flow fields would probably show more resemblance but it would take longer for each optimization run to converge.

Looking at the velocity profiles in figure 5.6, it can first be said that the vertical velocities are very similar at all streamwise locations. At $x = 0$ mm and $x = 10$ mm, the horizontal velocity is higher for the optimized case than for the benchmark case, whereas at $x = 20$ mm, $x = 50$ mm and $x = 100$ mm the magnitude of the horizontal velocities seem to be quite similar. It is again clear that the jet is much thinner for the optimized case compared to the benchmark case, confirming the findings from the velocity fields in figure 5.5.

In conclusion, it can be said that the optimization procedure managed to achieve quite a good match in terms of the magnitude of the velocity at different streamwise locations. Also the maximum velocities in x-direction and the minimum velocities in y-direction are well matched. Where the optimization failed is the location and thickness of the produced jet, as the jet is closer to the plate for the optimized velocity field compared to the benchmark velocity field.

5.3 Body force fields and pressure gradients

After having analysed the integral force components and the resemblance between the optimized velocity field and the benchmark velocity field, the optimized body force fields will be discussed together with the pressure gradients in the region where the body force is applied. The body force fields and pressure gradients for different peak-to-peak voltage amplitudes are displayed in figure 5.7 whereas the the same data is displayed for different voltage frequencies in figure 5.8. Furthermore, the maximum body force density in N/m^3 and the maximum pressure gradient in Pa/m (which is equivalent to N/m^3 since 1 Pa = 1 N/m^2) are summarized in table 5.2 and table 5.3 for different voltage amplitudes and voltage frequencies respectively.

Looking at figure 5.7, it can be noticed that all the body force fields are quite similar except for the case where the voltage amplitude is 8 kV. This is due to the fact that the optimization routine found a global minimum starting from another initial point for 8 kV than it did for 10, 12, 14 and 16 kV. Whether the body force fields displayed here are indeed global minima and not local minima cannot be said with certainty, but given the fact that not all body force fields have a similar shape it is likely that the optimization routine found a local minimum

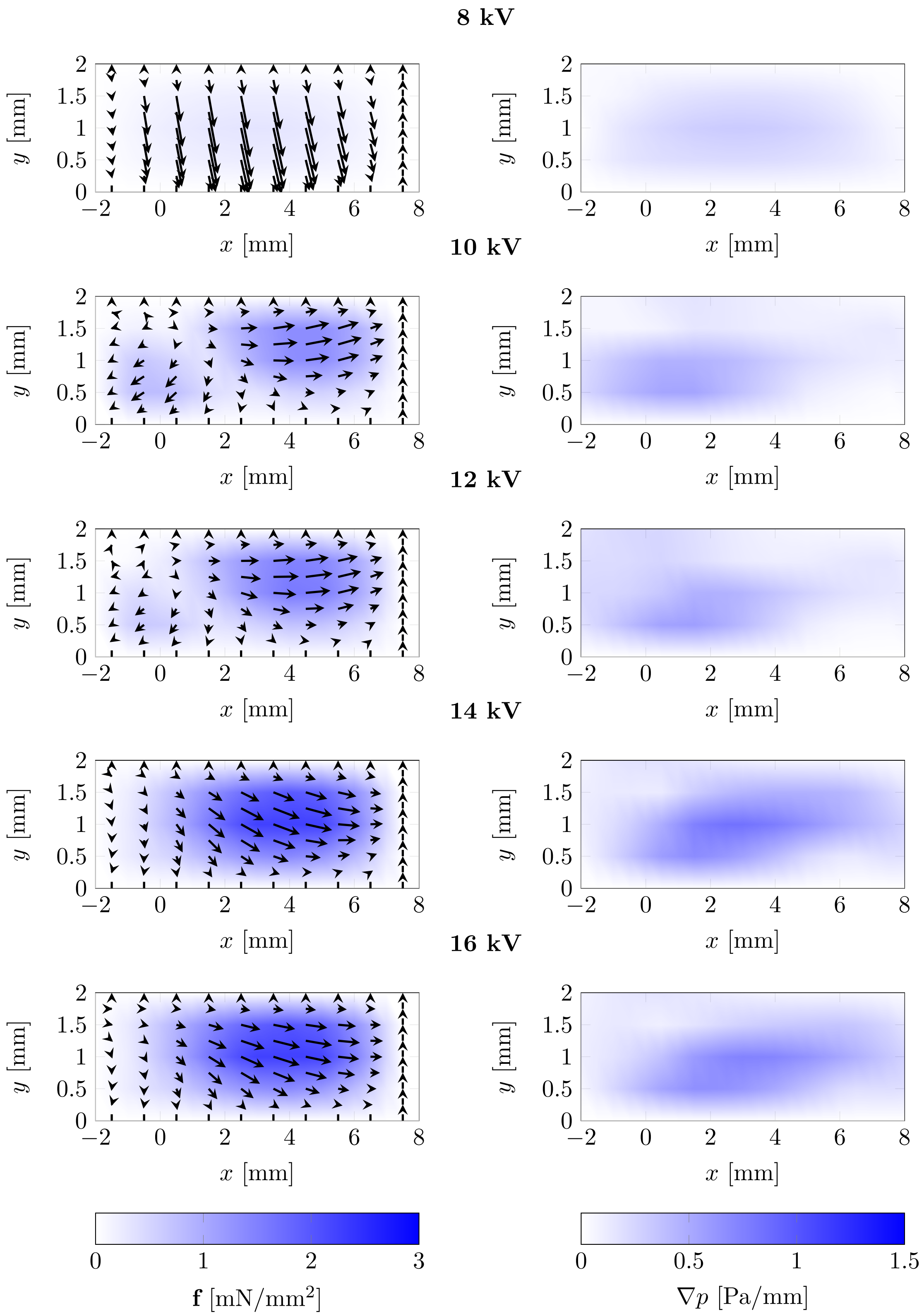

Figure 5.7: Optimized body force fields and pressure gradients for different voltage amplitudes and a voltage frequency of 2 kHz.

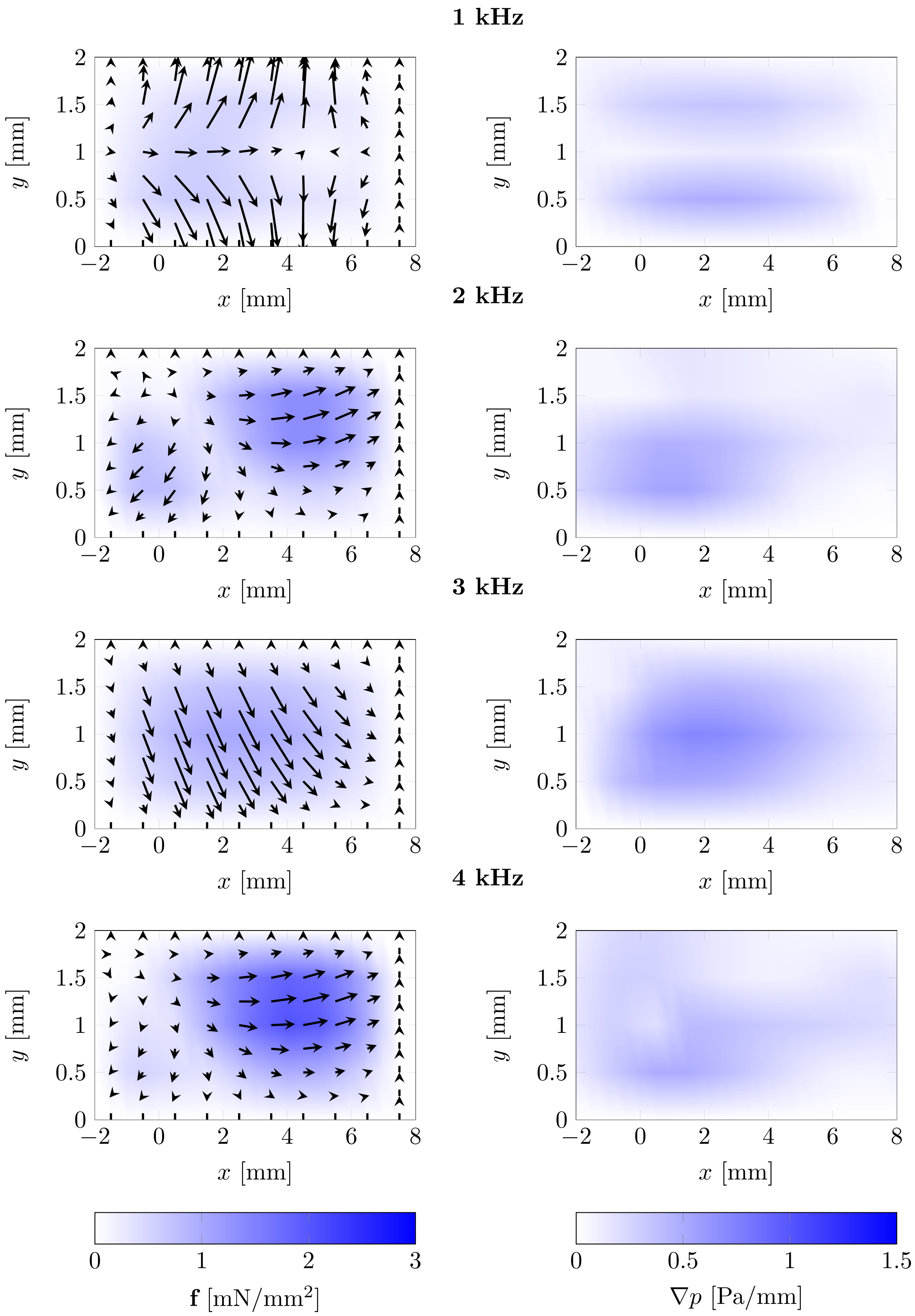

Figure 5.8: Optimized body force fields and pressure gradients for different voltage frequencies and a voltage amplitude of 10 kV.

Table 5.2: Maximum body force density and maximum pressure gradient for different voltage amplitudes and a voltage frequency of 2 kHz.

voltage amplitude	max. body force density	max. pressure gradient
8 kV	416.0 N/m^3	411.5 Pa/m
10 kV	2038.8 N/m^3	767.7 Pa/m
12 kV	2308.6 N/m^3	784.3 Pa/m
14 kV	3258.8 N/m^3	1114.7 Pa/m
16 kV	3302.6 N/m^3	1027.2 Pa/m

Table 5.3: Maximum body force density and maximum pressure gradient for different voltage frequencies and a voltage amplitude of 10 kV.

voltage frequency	max. body force density	max. pressure gradient
1 kHz	834.1 N/m^3	640.6 Pa/m
2 kHz	2038.8 N/m^3	767.7 Pa/m
3 kHz	1397.2 N/m^3	949.9 Pa/m
4 kHz	2901.8 N/m^3	698.4 Pa/m

instead of the global minimum in some cases. It is clear however that the magnitude of the body force increases with increasing voltage amplitude. Looking at the maximum body force density and maximum pressure gradient in table 5.2, it can be said that the pressure gradient is certainly of the same order of magnitude as the body force density.

Turning to figure 5.8, it can again be noticed that the optimal body force field was found starting from different initial points. Only for 2 and 4 kHz, the same starting point was used. When looking at table 5.3, the maximum body force density increases with increasing voltage frequency except for a voltage frequency of 3 kHz. Since another starting point was used to reach the optimal body force distribution in this case, the body force is more spread out over the body force field. Therefore, the maximum body force density is lower although the total force in x-direction follows the linear trend in figure 5.2. Again, the maximum pressure gradient is of the same order of magnitude as the maximum body force density.

Looking at the distribution of the body force in both figure 5.7 and figure 5.8 and comparing to the distributions found previously by Kotsonis et al [30] and Kriegseis et al [31], there is not much resemblance to be found. This is due to the fact that the body force field had to be parametrized using a Bézier surface and that the number of control points had to be limited to 3×2 control points in order to be able to perform the optimization in a reasonable amount of time. The accuracy of the distribution of the body force will probably be higher when more control points can be used or, ideally, when every node can be optimized individually.

The fact that different starting points have been used by the `MultiStart` algorithm to find the optimal body force distribution for each case points to the fact that the global minimum might not have been found for every case. Since the research was subjected to time constraints, only 10 different starting points have been used by `fmincon` to find a local minimum. If none of the starting points lie within the same basin of attraction as the global minimum, only local minima have been found and more starting points should be evaluated to reach the global minimum.

Chapter 6

Conclusions & recommendations

Although numerous simplifications had to be made in order to perform the optimization of the body force field in a reasonable amount of time, some valuable conclusions can be drawn from the results presented in the previous chapter. First of all, although the difference between the optimized velocity field and the benchmark velocity field is quite large, the optimization managed to match the maximum velocity in x-direction and the minimum velocity in y-direction quite closely as can be seen in figure 5.3 and figure 5.4. Also the magnitude of the velocity at different streamwise locations is quite accurate (figure 5.6, although the jet is thinner and closer to the plate than it should be.

Furthermore, the integral body force in x-direction displays valid behaviour with both increasing voltage amplitude (figure 5.1) and with increasing voltage frequency (see figure 5.2). For increasing voltage amplitude, the integral body force in x-direction seems to increase according to a power law while for increasing voltage frequency, f_x seems to increase linearly. Similar behaviour has also been found by other researchers for both increasing voltage amplitude and voltage frequency. The integral force in y-direction shows no clear trend for increasing voltage amplitude or voltage frequency, so no clear conclusions can be drawn with regard to f_y.

Due to the parametrization of the body force field, the distribution of the body force in the region where the body force is applied is not really detailed. It is also not clear which (if any) distribution is the optimal distribution, as the optimal body force field was obtained starting from different initial optimization points for different cases (figures 5.7 and 5.8). No clear conclusions can thus be drawn with regard to the distribution of the body force in space.

Lastly, comparing the magnitude of the body force density and the magnitude of the pressure gradient in the region where the body force is applied, it can be seen in table 5.2 and 5.3 that the magnitude of the pressure gradient is of the same order as the magnitude of the body force. Therefore, this research challenges the validity of obtaining the body force generated by a plasma actuator by using velocity data and neglecting the pressure gradient, as proposed by Wilke [63] and used in practice by many other researchers. The pressure gradient is far from negligible according to the current research and should thus not be disregarded at all.

For future research on the optimization of the body force field generated by a plasma actuator, it is suggested first of all to increase the number of control points of the Bézier surface in order to increase the accuracy of the distribution of the body force. Also the region where the body force is applied can be enlarged to see whether the body force maybe applies over a larger region or if it is indeed constrained to the region defined in this research. Of course, a refinement of the grid and, if possible, the use of a second order scheme instead of an upwind scheme is equally recommended.

Since it is not clear whether the optimization routine found global minima or local minima, more starting points should be used from which `fmincon` can try to find the global minimum. Another option is to investigate the use of the `GlobalSearch` algorithm, since using this algorithm should increase the chance that the global minimum is found. This was not possible in the current research due to time constraints. Also the use of a different optimization objective should be explored, as in this research the mean of the difference between the optimized field and the benchmark field is used. This allows for a faster optimization but has the risk that a large difference in one region is compensated by another large, but opposite difference in another region. Trying to minimize the maximum velocity difference should result in a better match between the optimized and the benchmark velocity fields, but will take more time to converge.

Lastly, the variation of the body force field during the AC voltage cycle can be investigated by optimizing the body force field at several points in the cycle, provided that velocity data is available at several points in the cycle from e.g. time-resolved PIV measurements. This could give an insight into whether the body force exhibits Push-pull or Push-push behaviour, i.e. whether the body force is positive in x-direction throughout the complete voltage cycle or changes direction as it proceeds through the different phases of this cycle.

References

[1] T. Abe, Y. Takizawa, S. Sato, and N. Kimura. Experimental study for momentum transfer in a dielectric barrier discharge plasma actuator. *AIAA Journal*, 46(9):2248–2256, 2008.

[2] J. Agnarsson, M. Sunde, and I. Ermilova. Parallel optimization in matlab. Report, Uppsala University, 2013.

[3] T. Albrecht, T. Weier, G. Gerbeth, H. Metzkes, and J. Stiller. A method to estimate the planar, instantaneous body force distribution from velocity field measurements. *Physics of Fluids*, 23(2), 2011.

[4] A. Bar-Sever. Separation control on an airfoil by periodic forcing. *AIAA journal*, 27(6):820–821, 1989.

[5] N. Benard, A. Debien, and E. Moreau. Time-dependent volume force produced by a non-thermal plasma actuator from experimental velocity field. *Journal of Physics D-Applied Physics*, 46(24), 2013.

[6] N. Benard, J. Jolibois, and E. Moreau. Lift and drag performances of an axisymmetric airfoil controlled by plasma actuator. *Journal of Electrostatics*, 67(2-3):133–139, 2009.

[7] L. N. Cattafesta and M. Sheplak. Actuators for active flow control. *Annual Review of Fluid Mechanics*, 43(1):247–272, 2011.

[8] T. C. Corke, C. L. Enloe, and S. P. Wilkinson. *Dielectric Barrier Discharge Plasma Actuators for Flow Control*, volume 42, pages 505–529. Annual Reviews, Palo Alto, 2010.

[9] T. C. Corke and E. Matlis. Phased plasma arrays for unsteady flow control. *AIAA paper*, 2323:1–10, 2000.

[10] T. C. Corke and M. L. Post. Overview of plasma flow control: Concepts, optimization, and applications. In *43rd AIAA Aerospace Sciences Meeting and Exhibit*, pages 13205–13219, 2005.

[11] T. C. Corke, M. L. Post, and D. M. Orlov. Single dielectric barrier discharge plasma enhanced aerodynamics: physics, modeling and applications. *Experiments in Fluids*, 46(1):1–26, 2008.

[12] R. Courant, K. Friedrichs, and H. Lewy. On the partial difference equations of mathematical physics. *IBM journal of Research and Development*, 11(2):215–234, 1967.

[13] T. Crittenden, A. Glezer, R. Funk, and D. Parekh. Combustion-driven jet actuators for flow control. *AIAA paper*, 2768:2001, 2001.

[14] A. Debien, N. Benard, L. David, and E. Moreau. Unsteady aspect of the electrohydrodynamic force produced by surface dielectric barrier discharge actuators. *Applied Physics Letters*, 100(1), 2012.

[15] C. L. Enloe, G. I. Font, T. E. McLaughlin, and D. M. Orlov. Surface potential and longitudinal electric field measurements in the aerodynamic plasma actuator. *AIAA Journal*, 46(11):2730–2740, 2008.

[16] C. L. Enloe, T. E. McLaughlin, R. D. VanDyken, K. D. Kachner, E. J. Jumper, and T. C. Corke. Mechanisms and responses of a single dielectric barrier plasma actuator: Plasma morphology. *AIAA Journal*, 42(3):589–594, 2004.

[17] C. L. Enloe, T. E. McLaughlin, R. D. VanDyken, K. D. Kachner, E. J. Jumper, T. C. Corke, M. Post, and O. Haddad. Mechanisms and responses of a single dielectric barrier plasma actuator: Geometric effects. *AIAA Journal*, 42(3):595–604, 2004.

[18] H. E. Fiedler and H. H. Fernholz. On management and control of turbulent shear flows. *Progress in Aerospace Sciences*, 27(4):305–387, 1990.

[19] M. Gad-el Hak. Modern developments in flow control. *Applied Mechanics Reviews*, 49(7):365–379, 1996.

[20] A. Glezer and M. Amitay. Synthetic jets. *Annual Review of Fluid Mechanics*, 34:503–529, 2002.

[21] C. He, T. C. Corke, and M. P. Patel. Plasma flaps and slats: An application of weakly ionized plasma actuators. *Journal of Aircraft*, 46(3):864–873, 2009.

[22] A. Hendra and S. Adinugroho. Matlab solvers benchmark for abb's model predictive control optimization. Report, Uppsala University, 2015.

[23] J. H. Huang, T. C. Corke, and F. O. Thomas. Unsteady plasma actuators for separation control of low-pressure turbine blades. *AIAA Journal*, 44(7):1477–1487, 2006.

[24] T. N. Jukes, K. S. Choi, G. A. Johnson, and S. J. Scott. Characterization of surface plasma-induced wall flows through velocity and temperature measurements. *AIAA Journal*, 44(4):764–771, 2006.

[25] T. N. Jukes, K. S. Choi, G. A. Johnson, and S. J. Scott. Turbulent drag reduction by surface plasma through spanwise flow oscillation. *AIAA paper*, 3693, 2006.

[26] Y. Katz, B. Nishri, and I. Wygnanski. The delay of turbulent boundary layer separation by oscillatory active control. *Physics of Fluids A: Fluid Dynamics (1989-1993)*, 1(2):179–181, 1989.

[27] C. J. Khler, S. Scharnowski, and C. Cierpka. On the uncertainty of digital piv and ptv near walls. *Experiments in Fluids*, 52(6):1641–1656, 2012.

[28] C. Kim, W. P. Jeon, J. Park, and H. Choi. Effect of a localized time-periodic wall motion on a turbulent boundary layer flow. *Physics of Fluids*, 15(1):265–268, 2003.

[29] M. Kotsonis. Diagnostics for characterisation of plasma actuators. *Measurement Science and Technology*, 26(9), 2015.

[30] M. Kotsonis, S. Ghaemi, L. Veldhuis, and F. Scarano. Measurement of the body force field of plasma actuators. *Journal of Physics D-Applied Physics*, 44(4), 2011.

[31] J. Kriegseis, C. Schwarz, C. Tropea, and S. Grundmann. Velocity-information-based force-term estimation of dielectric-barrier discharge plasma actuators. *Journal of Physics D-Applied Physics*, 46(5), 2013.

[32] I. Langmuir. The interaction of electron and positive ion space charges in cathode sheaths. *Physical Review*, 33(6):954–989, 1929.

[33] S. Leonov, D. Opaits, R. Miles, and V. Soloviev. Time-resolved measurements of plasma-induced momentum in air and nitrogen under dielectric barrier discharge actuation. *Physics of Plasmas*, 17(11), 2010.

[34] J. C. Lin, S. K. Robinson, R. J. Mcghee, and W. O. Valarezo. Separation control on high-lift airfoils via micro-vortex generators. *Journal of Aircraft*, 31(6):1317–1323, 1994.

[35] J. Little, M. Nishihara, I. Adamovich, and M. Samimy. High-lift airfoil trailing edge separation control using a single dielectric barrier discharge plasma actuator. *Experiments in Fluids*, 48(3):521–537, 2009.

[36] E. Moreau. Airflow control by non-thermal plasma actuators. *Journal of Physics D-Applied Physics*, 40(3):605–636, 2007.

[37] J. P. Murphy and P. Lavoie. Characterization of dbd plasma actuators via piv measurements. In *51st AIAA Aerospace Sciences Meeting including the New Horizons Forum and Aerospace Exposition 2013*.

[38] V. Narayanaswamy, L. L. Raja, and N. T. Clemens. Characterization of a high-frequency pulsed-plasma jet actuator for supersonic flow control. *AIAA Journal*, 48(2):297–305, 2010.

[39] M. Neumann, C. Friedrich, J. Czarske, J. Kriegseis, and S. Grundmann. Determination of the phase-resolved body force produced by a dielectric barrier discharge plasma actuator. *Journal of Physics D-Applied Physics*, 46(4), 2013.

[40] OpenFOAM foundation. Features of OpenFOAM. http://www.openfoam.org/features/, 2011. Accessed: 9-12-2014.

[41] M. L. Post. *Plasma Actuators for Separation Control on Stationary and Oscillating Airfoils*. Ph.d. thesis, 2004.

[42] G. D. Raithby. A critical evaluation of upstream differencing applied to problems involving fluid flow. *Computer Methods in Applied Mechanics and Engineering*, 9(1):75–103, 1976.

[43] L. F. Richardson and J. A. Gaunt. The deferred approach to the limit. part i. single lattice. part ii. interpenetrating lattices. *Philosophical Transactions of the Royal Society of London Series a-Containing Papers of a Mathematical or Physical Character*, 226:299–361, 1927.

[44] J. R. Roth and D. Xin. *Optimization of the Aerodynamic Plasma Actuator as an Electrohydrodynamic (EHD) Electrical Device*. Aerospace Sciences Meetings. American Institute of Aeronautics and Astronautics, 2006.

[45] D. V. Roupassov, A. A. Nikipelov, M. M. Nudnova, and A. Y. Starikovskii. Flow separation control by plasma actuator with nanosecond pulsed-periodic discharge. *AIAA Journal*, 47(1):168–185, 2009.

[46] C. J. Roy. Review of code and solution verification procedures for computational simulation. *Journal of Computational Physics*, 205(1):131–156, 2005.

[47] M. Samimy, I. Adamovich, B. Webb, J. Kastner, J. Hileman, S. Keshav, and P. Palm. Development and characterization of plasma actuators for high-speed jet control. *Experiments in Fluids*, 37(4):577–588, 2004.

[48] A. Seifert, T. Bachar, D. Koss, M. Shepshelovich, and I. Wygnanski. Oscillatory blowing - a tool to delay boundary-layer separation. *Aiaa Journal*, 31(11):2052–2060, 1993.

[49] A. Seifert, A. Darabi, and I. Wygnanski. Delay of airfoil stall by periodic excitation. *Journal of Aircraft*, 33(4):691–698, 1996.

[50] A. Seifert, S. Eliahu, D. Greenblatt, and I. Wygnanski. Use of piezoelectric actuators for airfoil separation control. *AIAA journal*, 36(8):1535–1537, 1998.

[51] K. P. Singh and S. Roy. Physics of plasma actuator operating in atmospheric air. *Applied Physics Letters*, 92(11), 2008.

[52] V. R. Soloviev. Analytical estimation of the thrust generated by a surface dielectric barrier discharge. *Journal of Physics D-Applied Physics*, 45(2), 2012.

[53] B. L. Storms and C. S. Jang. Lift enhancement of an airfoil using a gurney flap and vortex generators. *Journal of Aircraft*, 31(3):542–547, 1994.

[54] The Mathworks, Inc. MATLAB documentation. http://nl.mathworks.com/help/. Accessed: 20-10-2015.

[55] C. Thill, J. Etches, I. Bond, K. Potter, and P. Weaver. Morphing skins. *The Aeronautical Journal*, 112(1129):117–139, 2008.

[56] F. O. Thomas, T. C. Corke, M. Iqbal, A. Kozlov, and D. Schatzman. Optimization of dielectric barrier discharge plasma actuators for active aerodynamic flow control. *AIAA Journal*, 47(9):2169–2178, 2009.

[57] F. O. Thomas, A. Kozlov, and T. C. Corke. Plasma actuators for cylinder flow control and noise reduction. *AIAA Journal*, 46(8):1921–1931, 2008.

[58] H. K. Versteeg and W. Malalasekera. *An Introduction to Computational Fluid Dynamics: The Finite Volume Method*. Pearson Education Limited, 2007.

[59] H. Viets, M. Piatt, and M. Ball. Boundary-layer control by unsteady vortex generation. *Journal of Wind Engineering and Industrial Aerodynamics*, 7(2):135–144, 1981.

[60] V. Voikov, T. C. Corke, and O. Haddad. Numerical simulation of flow control over airfoils using plasma actuators. In *APS Division of Fluid Dynamics Meeting Abstracts*, volume 1, 2004.

[61] A. N. Vorobiev, R. M. Rennie, E. J. Jumper, and T. E. McLaughlin. Experimental investigation of lift enhancement and roll control using plasma actuators. *Journal of Aircraft*, 45(4):1315–1321, 2008.

[62] R. D. Whalley and K. S. Choi. Turbulent boundary-layer control with spanwise travelling waves. *13th European Turbulence Conference (Etc13): Wall-Bounded Flows and Control of Turbulence*, 318(2), 2011.

[63] J. B. Wilke. Aerodynamic flow-control with dielectric barrier discharge plasma actuators. In *DLR Deutsches Zentrum fur Luft- und Raumfahrt e.V. - Forschungsberichte*. 2009.

[64] S. P. Wilkinson. Investigation of an oscillating surface plasma for turbulent drag reduction. *AIAA paper*, 1023, 2003.

[65] P. F. Zhang, B. Yan, A. B. Liu, and J. J. Wang. Numerical simulation on plasma circulation control airfoil. *AIAA Journal*, 48(10):2213–2226, 2010.